A non-periodic two scale asymptotic method to take account of rough topographies for 2D elastic wave propagation

Yann Capdeville, Jean-Jacques Marigo

Geophys. J. Int. (2010) **000,** 000–000

A non-periodic two scale asymptotic method to take account of rough topographies for 2D elastic wave propagation

Yann CAPDEVILLE[1], Jean-Jacques MARIGO[2]

[1] *LPGNantes (UMR 6612), CNRS.* email: yann.capdeville@univ-nantes.fr

[2] *Laboratoire de Mécanique des solides (UMR 7649), École Polytechnique*

keywords: Wave propagation, Theoretical Seismology, Computational seismology, topography, wave scattering and diffraction, numerical solutions.
18 September 2012

SUMMARY

We propose a two scale asymptotic method to compute the effective effect of a free surface topography varying much faster than the minimum wavelength for 2-D P-SV elastic wave propagation. The topography variation is assumed to be non-periodic but with a deterministic description and, in the present paper, the elastic body below the topography is assumed to be homogeneous. Two asymptotic expansions are used, one in the boundary layer close to the free surface and one in the volume. Both expansions are matched appropriately up to the order 1 to provide an effective topography and an effective boundary condition. We show that the effective topography is not the averaged topography but it is a smooth free surface lying below the fast variations of the real topography. Moreover, the free boundary condition has to be modified to take account of the inertial effects of the fast variations of the topography above the effective topography. In other words, the wave is not propagating in the fast topography but below it and is slowed down by the weight of the fast topography. We present an iterative scheme allowing to find this effective topography for a given minimum wavelength. We do not attempt any mathematical proof of the proposed scheme, nevertheless, numerical tests show good results.

1 INTRODUCTION

Because it controls surface waves and because sources and receivers are often in its neighborhood, the free surface is an important boundary for elastic wave propagation, especially for seismology. For the forward problem, the free surface is a well known difficulty for strong form numerical methods like the finite differences . For numerical methods based on the weak form of the wave equation, like, for example, the Spectral Element Method (SEM, e.g. Komatitsch & Vilotte (1998) or Chaljub *et al.* (2007) for a review), the free surface with its topography is not an issue as long as it can efficiently be meshed. For the inverse problem, the topography of the free surface is most of the time ignored and assumed to be flat (or spherical for the global earth). The impact of such an assumption is assumed to be weak, but its effects have been little studied, even if some works exist (e.g. Köhler *et al.* 2012). Most of the time, in seismology and in almost any field involving acoustic or elastic waves, because it can be measured directly with optical methods, the free surface topography is well known, and to a much finer scale than the minimum wavelength λ_m considered. A consequence of this detailed description of the topography, is that, for both forward and inverse problems, it needs to be upscaled. Indeed, a detailed topography to scales much finer than the minimum wavelength leads to a numerical over-cost. To solve this problem, the topography is in most of the cases smoothed with a lowpath filter, which is a trivial upscaling method. To our knowledge, the impact of such a filtering on wave propagation has not been studied. The objective of this paper is to develop a method to upscale rough topographies compared to the minimum wavelength, in a consistent way with respect to the wave equation.

The problem of rough topography for elastic waves is very similar to the problem of small inclusions or damages close to an interface which has been studied for long for the static and periodic cases with two scale approaches by the solid mechanics community (Sanchez-Palencia, 1986; Dumontet, 1990; Nevard & Keller, 1997; Marigo & Pideri, 2011; David *et al.*, 2012). These works are the base of the present paper. The non-periodic static case has been addressed mathematically by several authors (Chechkin *et al.*, 1996; Eger *et al.*, 2000). If these works give an idea of the type of convergence we can expect for an asymptotic method in such a case, they are not really helping to solve the problem in practice for a given topography. For the dynamic case, periodic topographies and stochastic topographies have been studied by Huang & Maradudin (1987), Mayer *et al.* (1991) and Maradudin *et al.* (1991). An example of a two scale approach for the dynamic case in a presence of a fast boundary condition can be found in Boutin & Roussillon (2006) and the case of non-periodic fast variations, but in a single direction, close to the free surface has been studied by Capdeville & Marigo (2008). To our knowledge, no results can be found for the non-periodic deterministic case.

The outline of this paper is as follows. In Sec. 2, we present the asymptotic method for a periodic fast topography above an homogeneous body, which is a classical development, following Marigo &

Pideri (2011) and David *et al.* (2012). The idea is to use two asymptotic solutions, one valid in the boundary layer close to the free surface and one valid in the volume. The boundary layer asymptotic solution satisfies exactly the free surface condition with rapid variations, which is not the case of the asymptotic solution valid in the volume. The two asymptotic solutions are matched in the region where they are both valid and, once matched, the boundary layer asymptotic solution provides the boundary condition for the free surface for the asymptotic solution in the volume. We show that, to the order 1, the topography is equivalent to a flat effective topography and a dynamic boundary condition. We then perform some validation and convergence tests that show that the wave is not propagating into the rapid variations of the topography but just below it and that only the weight of the rapid variation of the fast topography is slowing down the surface wave. In Sec. 3, we propose an extension of the periodic development to the non-periodic case, following the principles proposed by Capdeville & Marigo (2007), Capdeville *et al.* (2010a), Guillot *et al.* (2010), and Capdeville *et al.* (2010b), and we propose an iterative algorithm to find an appropriate effective topography and boundary conditions. We draw the same conclusion as for the periodic case that the surface wave is not propagating into the rapid variations of the topography but just below it and is affected by its weight. We finally present some validation tests using three different topographies.

2 PERIODIC CASE

In this section, we present the two scale approach for a periodic fast scale topography following Marigo & Pideri (2011) and David *et al.* (2012). Some aspects of the employed notations are given in appendix A.

Before we start, let us give an handwaving introduction to what follows. If two scale homogenization approaches are well known in the solid mechanics community, they are relatively technical and non trivial methods and not so well known in the geophysical community. The main ideas of the two scale method presented here are the following: for the periodic case, it is first assumed that the two scales are present in the problem. One of the two scales, the microscopic scale, is the periodicity of the topography and the other one, the macroscopic scale, is the wavelength of the propagating wavefield. The two scale homogenization solution is an asymptotic solution controlled by a small parameter ε which is the ratio of the small periodicity versus the large wavelength. Two points are unusual for many of us with this kind of method.

First, it explicitly takes into account the small scales by introducing a new space variable (usually $\mathbf{y}$), named the microscopic variable, which is a zoom by $1/\varepsilon$ of the classical space variable $\mathbf{x}$ also named the macroscopic variable. Assuming the two variables are independent, from the original wave equations is built a new set of equations to be solved to find the coefficients of the homoge-

nized asymptotic expansion. These new equations depend upon the two space variables which can be puzzling, but only one value of microscopic variable has a physical meaning: $\mathbf{y} = \mathbf{x}/\varepsilon$.

Second, even if the considered real case correspond to a fixed value of ε (there is only one value for the periodicity and for the minimum wavelength), say $\varepsilon = \varepsilon_r$, ε is made variable and the convergence can only be achieved when ε goes to zero. Indeed, from the real problem are built a series of problem by varying the periodicity size and keeping the minimum wavelength constant and therefore allowing the value of ε to vary. The real case is only a particular case of the series and is obtained for $\varepsilon = \varepsilon_r$. This can be disturbing to allow ε to vary knowing the real case correspond to a fixed value of ε, but it is the way two scale homogenization methods are built. If $\mathbf{u}^\varepsilon$ is the displacement solution to the classical wave equation in the media containing the small scale and $\mathbf{u}^0$ the leading term of the homogenized asymptotic solution, an important result of the two scale homogenization theory is to demonstrate the convergence of $\mathbf{u}^\varepsilon$ toward $\mathbf{u}^0$ when ε goes to zero. In a sense, because ε_r is different from zero, the real case is an approximation of the homogenized solution. Of course, things can be presented differently and the homogenized solution can be seen has an approximate solution of the real case. A practical consequence of this is that if it happens that ε_r is not small enough, $\mathbf{u}^0$ might be significantly different from $\mathbf{u}^{\varepsilon_r}$ and little can be done to improve the solution in such a case (adding more term of the series can help, but not very far). In other words, as the order 0 homogenized solution does not depend upon ε, there is always a real topography for which the value of ε_r is large enough so that the homogenized solution doesn't approximate correctly the real solution. We will nevertheless see that non-periodic homogenization can be a solution to that problem.

For the fast topography problem presented here, two asymptotic expansion are used. One valid close to the free surface, in the boundary layer, and one valid far away from the free surface, in the volume. The two solutions are assumed to be both valid in a region between the volume and the boundary layer where they are matched. The volume solution is the solution that will be used to actually propagate waves in a medium with an approximate topography but the boundary layer solution is the only one that exactly satisfies the boundary condition on the rapid topography. Through the matching conditions, the boundary layer solution provides the missing consistent boundary condition for the volume solution. The main result of this section is quite simple: the small scale problem can be replaced by an approximate problem for which the topography is flat and lying below the real topography. More over, the usual zero traction boundary condition is replaced by a dynamic boundary condition to account for the mass of the material that is over the flat effective topography and that is now missing

Figure 1. Two examples of periodic boundaries $\mathbf{\Gamma}^\varepsilon$. Only the right one can be written as $\mathbf{\Gamma}^\varepsilon = \{\mathbf{x} \in \mathbb{R}^2 \; ; \; x_1 = \Gamma^\varepsilon(x_2)\}$. The grey line is the x_2 axis and $\mathbf{\Gamma}_s$. The dashed lines are the average interface height.

2.1 Settings

We consider a two-dimensional infinite elastic half space $\mathbf{\Omega}^\varepsilon$ with a rough boundary $\mathbf{\Gamma}^\varepsilon$. In this paper, the density ρ and fourth order elastic tensor $\mathbf{c}$ are assumed to be constant and we leave the inhomogeneous case for future works. $\mathbf{\Omega}^\varepsilon$ is subject to an external source force $\boldsymbol{f} = \boldsymbol{f}(\mathbf{x}, t)$ and we wish to study the displacement $\mathbf{u}^\varepsilon(\mathbf{x}, t) = u_i^\varepsilon(\mathbf{x}, t)\, \hat{\mathbf{x}}_i$, where $\hat{\mathbf{x}}_i$, $i = 1, 2$ are the unit vectors of the Cartesian coordinate system, induced by $\boldsymbol{f}$. We assume that $\boldsymbol{f}(\mathbf{x}, t)$ has a maximum frequency f_c which allows to assume that, in the far field, it exists a minimum wavelength λ_m to the wavefield $\mathbf{u}^\varepsilon$. In this section, $\mathbf{\Gamma}^\varepsilon$ is assumed to be periodic of periodicity l and with a maximum amplitude variation e (see Fig. 1). ε characterizes $\mathbf{\Gamma}^\varepsilon$ periodicity l with respect to λ_m:

$$\varepsilon = \frac{l}{\lambda_m} \,. \tag{1}$$

As mentioned in the previous section, the two scale homogenization method requires to make vary the periodicity, and therefore ε, which explains why most of the quantities used here depends upon ε. In some cases, $\mathbf{\Gamma}^\varepsilon$ can be written as $\mathbf{\Gamma}^\varepsilon = \{\mathbf{x} \in \mathbb{R}^2 \; ; \; x_1 = \Gamma^\varepsilon(x_2)\}$ and in such cases, $\mathbf{\Omega}^\varepsilon = \{\mathbf{x} \in \mathbb{R}^2 \; ; \; x_1 \geq \Gamma^\varepsilon(x_2)\}$ (see Fig. 1, right plot). Even if this is not true in general (e.g. Fig. 1, left plot), in the following, for the sake of simplicity, we assume it is the case, without losing the generality of the results. We define the generic function Γ such that, for any ε,

$$\varepsilon\Gamma(x_2/\varepsilon) \equiv \Gamma^\varepsilon(x_2) \,. \tag{2}$$

This definition of Γ is important. Indeed, it means that the ratio e over l in independent of ε. Therefore, when ε decreases, the periodicity of the topography is smaller as well as its amplitude. This is a necessary condition to show a convergence of the asymptotic solution presented here, at least for the order zero (Sanchez-Palencia, 1986; Eger *et al.*, 2000) and, for example, we cannot ensure convergence if only the periodicity l decreases with ε while keeping the amplitude e constant.

The displacement $\mathbf{u}^\varepsilon$ in $\mathbf{\Omega}^\varepsilon$ is driven by the elastic wave equation,

$$\begin{aligned} \rho\partial_{tt}\mathbf{u}^\varepsilon - \boldsymbol{\nabla}\cdot\boldsymbol{\sigma}^\varepsilon &= \boldsymbol{f} \quad \text{in} \quad \mathbf{\Omega}^\varepsilon \,, \\ \boldsymbol{\sigma}^\varepsilon &= \mathbf{c} : \boldsymbol{\epsilon}(\mathbf{u}^\varepsilon) \quad \text{in} \quad \mathbf{\Omega}^\varepsilon \,, \\ \boldsymbol{\sigma}^\varepsilon \cdot \mathbf{n}^\varepsilon &= \mathbf{0} \quad \text{on} \quad \mathbf{\Gamma}^\varepsilon \,, \end{aligned} \tag{3}$$

where $\mathbf{n}^\varepsilon$ is the outward normal to $\mathbf{\Gamma}^\varepsilon$ and where the component ij of the strain tensor is

$$[\boldsymbol{\epsilon}(\mathbf{u}^\varepsilon)]_{ij} \equiv \frac{1}{2}\left(\frac{\partial u_i^\varepsilon}{\partial x_j} + \frac{\partial u_j^\varepsilon}{\partial x_i}\right) . \tag{4}$$

The initial conditions for the displacement and velocity in $\mathbf{\Omega}^\varepsilon$ at $t = 0$ are assumed to be zero. Note that the infinite domain is in practice truncated thanks to absorbing boundary conditions.

2.2 Two scale asymptotic set up

We now assume that $\varepsilon \ll 1$, which means that the scale of the topography variations is much smaller that the minimum wavelength. As explained in the introduction section above, even if the real case defines a unique $\varepsilon = \varepsilon_r$, we allow ε to vary and set up an asymptotic expansion that can be shown to converge when $\varepsilon \to 0$ (Sanchez-Palencia, 1986). The real case is therefore an approximation to the two scale asymptotic solution presented here, whose accuracy depends on how small is ε_r. When ε varies, the displacement $\mathbf{u}^\varepsilon$ and the associate stress $\boldsymbol{\sigma}^\varepsilon$, solution to the wave equations (3), change, which is reminded with the ε superscript. We define $\mathbf{\Gamma}_s$, a flat interface parallel to $\mathbf{\Gamma}^\varepsilon$ (see Fig. 1) and we then set the origin of the coordinate system such that the x_2 axis is $\mathbf{\Gamma}_s$, that is $\mathbf{\Gamma}_s = \{\mathbf{x} \in \mathbb{R}^2 \; ; \; x_1 = 0\}$. If a is the average high of $\mathbf{\Gamma}^\varepsilon$, ($a = 1/l \int_0^l \Gamma^\varepsilon(x_2) dx_2$), we define $\mathbf{\Gamma}_a = \{\mathbf{x} \in \mathbb{R}^2 \; ; \; x_1 = a\}$ the average interface of $\mathbf{\Gamma}^\varepsilon$. If a is chosen to be zero, then $\mathbf{\Gamma}_s = \mathbf{\Gamma}_a$. We finally define $\mathbf{\Omega}_s$, the half plane below $\mathbf{\Gamma}_s$: $\mathbf{\Omega}_s = \{\mathbf{x} \in \mathbb{R}^2 \; ; \; x_1 \geq 0\}$.

In order to explicitly take small-scale boundary topography into account when solving the wave equation, the fast space variable is introduced:

$$\mathbf{y} = \frac{\mathbf{x}}{\varepsilon} . \tag{5}$$

We define the periodic cell, $\mathbb{Y}$ (see Fig. 2), the vertical domain below one periodic cell of the topography, zoomed by $1/\varepsilon$:

$$\mathbb{Y} = \{\mathbf{y} \in \mathbb{R} \times Y_w \; ; \; y_1 \geq \Gamma(y_2)\} , \tag{6}$$

where the segment

$$Y_w = \{y_2 \in [0, \lambda_m]\} . \tag{7}$$

The boundary of the periodic cell $\partial\mathbb{Y}$ is built of its top boundary $\mathbf{\Gamma}$, its left and right boundaries $\mathbf{Y}_1$ and $\mathbf{Y}_2$ and its lower boundary $\mathbf{Y}_3$ ($\partial\mathbb{Y} = \mathbf{Y}_1 \cup \mathbf{Y}_2 \cup \mathbf{Y}_3 \cup \mathbf{\Gamma}$). The $\mathbf{Y}_3$ boundary is set to the infinity in y_1. We define a partial periodic cell $\mathbb{Y}(b) = \{\mathbf{y} \in \mathbb{Y} \; ; \; y_1 < b\}$ which is the same domain as $\mathbb{Y}$, but with a lower boundary $\mathbf{Y}_3(b) = \{\mathbf{y} \in \mathbb{R}^2; y_1 = b \, , y_2 \in Y_w\}$ (we therefore have $\mathbb{Y} = \lim_{y_1 \to \infty} \mathbb{Y}(y_1)$). The width of the periodic cell in y_2 is $|Y_w| = \lambda_m$.

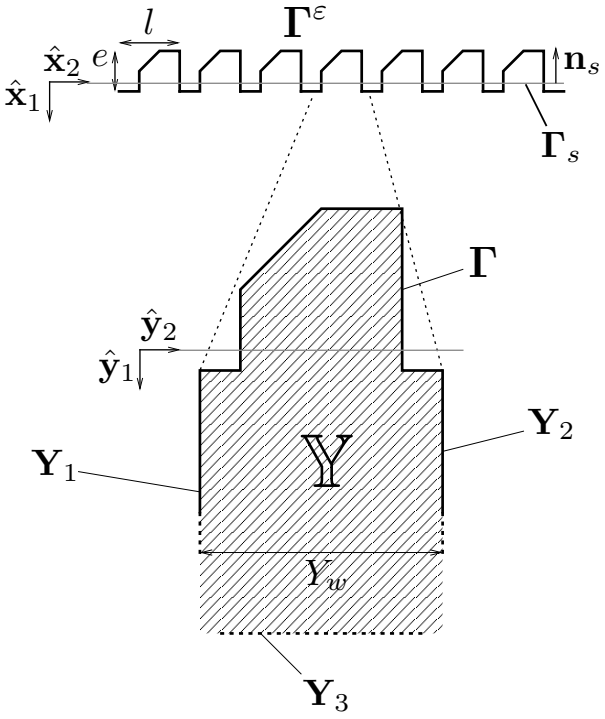

Figure 2. The periodic cell $\mathbb{Y}$, built from one periodic pattern of $\mathbf{\Gamma}^\varepsilon$ and expended with the transformation $\mathbf{y} = \mathbf{x}/\varepsilon$. The boundary of the periodic cell is $\partial\mathbb{Y} = \mathbf{Y}_1 \cup \mathbf{Y}_2 \cup \mathbf{Y}_3 \cup \mathbf{\Gamma}$ where the $\mathbf{Y}_3$ border is set to infinity in y_1.

Following a classical process (see e.g. Sanchez-Palencia 1986; Dumontet 1990; Marigo & Pideri 2011) we consider two asymptotic expansions for the solutions $(\mathbf{u}^\varepsilon, \boldsymbol{\sigma}^\varepsilon)$,

- the volume expansion, valid **away from $\mathbf{\Gamma}^\varepsilon$**, in $\mathbf{\Omega}_s$:

$$\begin{aligned}\mathbf{u}^\varepsilon(\mathbf{x}) &= \mathbf{u}^0(\mathbf{x}) + \varepsilon\mathbf{u}^1(\mathbf{x}) + \varepsilon^2\mathbf{u}^2(\mathbf{x}) + ...\\ \boldsymbol{\sigma}^\varepsilon(\mathbf{x}) &= \boldsymbol{\sigma}^0(\mathbf{x}) + \varepsilon\boldsymbol{\sigma}^1(\mathbf{x}) + \varepsilon^2\boldsymbol{\sigma}^2(\mathbf{x}) + ...\end{aligned} \tag{8}$$

- the boundary layer expansion, valid **close to $\mathbf{\Gamma}^\varepsilon$**, in $\mathbb{R} \times \mathbb{Y}$

$$\begin{aligned}\mathbf{u}^\varepsilon(\mathbf{x}) &= \mathbf{v}^0(x_2, \mathbf{y}) + \varepsilon\mathbf{v}^1(x_2, \mathbf{y}) + \varepsilon^2\mathbf{v}^2(x_2, \mathbf{y}) + ...\\ \boldsymbol{\sigma}^\varepsilon(\mathbf{x}) &= \frac{1}{\varepsilon}\boldsymbol{\tau}^{-1}(x_2, \mathbf{y}) + \boldsymbol{\tau}^0(x_2, \mathbf{y}) + \varepsilon\boldsymbol{\tau}^1(x_2, \mathbf{y}) + \varepsilon^2\boldsymbol{\tau}^2(x_2, \mathbf{y}) + ...\end{aligned} \tag{9}$$

The coefficients $\mathbf{v}^i$ and $\boldsymbol{\tau}^i$ are periodic in y_2 but not in y_1.

When $\varepsilon \to 0$, any change in $\mathbf{y}$ induces a very small change in $\mathbf{x}$. This leads to the separation of scales: **$\mathbf{y}$ and $\mathbf{x}$ are treated as independent variables**. This implies that partial derivatives with respect to $\mathbf{x}$ become:

$$\boldsymbol{\nabla}_\mathbf{x} \to \boldsymbol{\nabla}_\mathbf{x} + \frac{1}{\varepsilon}\boldsymbol{\nabla}_\mathbf{y}\,. \tag{10}$$

Similarly, we have, for the strain tensor:

$$\boldsymbol{\epsilon}_{\mathbf{x}} \to \boldsymbol{\epsilon}_{\mathbf{x}} + \frac{1}{\varepsilon}\boldsymbol{\epsilon}_{\mathbf{y}}\,. \tag{11}$$

The last equation explains why the stress expansion in (9) starts at $i = -1$ while the displacement expansion starts at $i = 0$. Indeed the relation between the stress and the displacement implies the strain tensor which contains a $1/\varepsilon$ factor. Consequently, the stress expansion starts one index earlier than the displacement.

In order to be matched, we assume that it exits a region where the two asymptotic expansions are valid. This region is close enough from $\boldsymbol{\Gamma}^{\varepsilon}$ so that x_1 can be considered as very small for the volume expansion and at the same time far enough so that y_1 can be considered as very large for the boundary layer expansion. Using that region where both expansions are valid, it is shown in appendix B that the matching conditions are:

$$\lim_{y_1\to+\infty}\left(\mathbf{v}^i(x_2,\mathbf{y}) - \sum_{j=0}^{i}\frac{y_1^{i-j}}{(i-j)!}\frac{\partial^{i-j}\mathbf{u}^j}{\partial x_1^{i-j}}(0,x_2)\right) = \mathbf{0}\,, \tag{12}$$

$$\lim_{y_1\to+\infty}\left(\boldsymbol{\tau}^i(x_2,\mathbf{y}) - \sum_{j=0}^{i}\frac{y_1^{i-j}}{(i-j)!}\frac{\partial^{i-j}\boldsymbol{\sigma}^j}{\partial x_1^{i-j}}(0,x_2)\right) = \mathbf{0}\,. \tag{13}$$

Following a classical development (e.g. Sanchez-Palencia 1986), introducing expansions (8) and (9) in the wave equations (3), using (10) and (11), identifying terms of the same power of ε yields the following coupled equations satisfied by the expansion coefficients of $(\mathbf{u}^{\varepsilon}, \boldsymbol{\sigma}^{\varepsilon})$:

- equations in the volume $\boldsymbol{\Omega}_s$, $i \in \mathbb{N}$:

$$\rho\partial_{tt}\mathbf{u}^i - \boldsymbol{\nabla}_{\mathbf{x}}\cdot\boldsymbol{\sigma}^i = \boldsymbol{f}\delta_{i0} \quad \text{in} \quad \boldsymbol{\Omega}_s\,, \tag{14}$$

$$\boldsymbol{\sigma}^i = \mathbf{c} : \boldsymbol{\epsilon}_{\mathbf{x}}\left(\mathbf{u}^i\right) \quad \text{in} \quad \boldsymbol{\Omega}_s \tag{15}$$

$$\lim_{x_1\to\infty}\boldsymbol{\sigma}^i\cdot\hat{\mathbf{x}}_1 = \mathbf{0}\,, \tag{16}$$

where δ_{ij} is the Kronecker symbol. Note that the usual top boundary condition is replaced by the matching conditions.

- equations in the boundary layer: for $i \geq -2$

$$\rho\partial_{tt}\mathbf{v}^i - \boldsymbol{\nabla}_{x_2}\cdot\boldsymbol{\tau}^i - \boldsymbol{\nabla}_{\mathbf{y}}\cdot\boldsymbol{\tau}^{i+1} = \boldsymbol{f}\delta_{i0} \quad \text{in} \quad \mathbb{R}\times\mathbb{Y}\,,\ i \geq -2\,, \tag{17}$$

$$\boldsymbol{\tau}^i = \mathbf{c} : \left(\boldsymbol{\epsilon}_{x_2}\left(\mathbf{v}^i\right) + \boldsymbol{\epsilon}_{\mathbf{y}}\left(\mathbf{v}^{i+1}\right)\right) \quad \text{in} \quad \mathbb{R}\times\mathbb{Y}\,,\ i \geq -1\,, \tag{18}$$

$$\boldsymbol{\tau}^i\cdot\mathbf{n} = \mathbf{0} \text{ on } \mathbb{R}\times\boldsymbol{\Gamma}\,,\ i \geq 0. \tag{19}$$

where $\mathbf{n}$ is the outward normal to $\partial\mathbb{Y}$.

- Matching conditions, here for the two first orders : For $(x_2, y_2) \in \mathbb{R} \times Y_w$

$$i = 0 \quad \begin{cases} \lim\limits_{y_1 \to +\infty} \left(\mathbf{v}^0(x_2, \mathbf{y}) - \mathbf{u}^0(0, x_2) \right) = 0 \\ \lim\limits_{y_1 \to +\infty} \left(\boldsymbol{\tau}^0(x_2, \mathbf{y}) - \boldsymbol{\sigma}^0(0, x_2) \right) = 0 \end{cases} \tag{20}$$

$$i = 1 \quad \begin{cases} \lim\limits_{y_1 \to +\infty} \left(\mathbf{v}^1(x_2, \mathbf{y}) - \mathbf{u}^1(0, x_2) - y_1 \dfrac{\partial \mathbf{u}^0}{\partial x_1}(0, x_2) \right) = 0 \\ \lim\limits_{y_1 \to +\infty} \left(\boldsymbol{\tau}^1(x_2, \mathbf{y}) - \boldsymbol{\sigma}^1(0, x_2) - y_1 \dfrac{\partial \boldsymbol{\sigma}^0}{\partial x_1}(0, x_2) \right) = 0 \end{cases} \tag{21}$$

2.3 Iterative resolution of the asymptotic equations

In this section, the asymptotic equations for the order 0 for the first order corrector are solved. The boundary conditions for the macroscopic equation in the volume are derived.

2.3.1 Order 0

We start by combining (17) for $i = -2$ and (18) for $i = -1$ to obtain:

$$\boldsymbol{\nabla}_{\mathbf{y}} \cdot \left(\mathbf{c} : \boldsymbol{\epsilon}_{\mathbf{y}}(\mathbf{v}^0) \right) = \mathbf{0} \,. \tag{22}$$

Taking the dot product of the last equation with $\mathbf{v}^0$, integrating over the periodic cell, then by parts and using the symmetry $c_{ijkl} = c_{klij}$, we obtain

$$\int_{\mathbb{Y}} \mathbf{v}^0 \cdot \boldsymbol{\nabla}_{\mathbf{y}} \cdot \left(\mathbf{c} : \boldsymbol{\epsilon}_{\mathbf{y}}(\mathbf{v}^0) \right) d\mathbf{y} = \int_{\partial \mathbb{Y}} \mathbf{v}^0 \cdot \boldsymbol{\tau}^{-1} \cdot \mathbf{n} \, d\mathbf{y} - \int_{\mathbb{Y}} \boldsymbol{\epsilon}_{\mathbf{y}}(\mathbf{v}^0) : \mathbf{c} : \boldsymbol{\epsilon}_{\mathbf{y}}(\mathbf{v}^0) \, d\mathbf{y} = 0 \,. \tag{23}$$

The integral over $\partial \mathbb{Y}$ in the last equation vanishes because the integral along $\boldsymbol{\Gamma}$ is zero thanks to the boundary conditions (19); the integrals over $\mathbf{Y}_1$ and $\mathbf{Y}_2$ (see Fig. 2) cancel themselves thanks to the periodicity in y_2; finally, the matching condition for $i = -1$ allows to find that $\boldsymbol{\tau}^{-1}(x_2, \infty, y_2) \cdot \hat{\mathbf{x}}_1 \to \boldsymbol{\sigma}^{-1}(0, x_2) \cdot \hat{\mathbf{x}}_1 = 0$ (indeed $\boldsymbol{\sigma}^i = 0$ for $i < 0$)) which implies that the integral over $\mathbf{Y}_3$ is also zero. Consequently, we have,

$$\int_{\mathbb{Y}} \boldsymbol{\epsilon}_{\mathbf{y}}(\mathbf{v}^0) : \mathbf{c} : \boldsymbol{\epsilon}_{\mathbf{y}}(\mathbf{v}^0) \, d\mathbf{y} = 0 \,, \tag{24}$$

which, knowing that $\mathbf{c}$ is a positive definite tensor, imposes that $\mathbf{v}^0$ is a constant translation plus a constant rotation in $\mathbf{y}$. The periodicity imposes that the constant rotation is zero and that $\mathbf{v}^0$ is a constant value for a fixed x_2. We therefore have

$$\mathbf{v}^0(x_2, \mathbf{y}) = \mathbf{v}^0(x_2) \,, \tag{25}$$

$$\boldsymbol{\tau}^{-1} = \mathbf{0} \,. \tag{26}$$

The order 0 matching condition for the displacement yields:

$$\mathbf{u}^0(0, x_2) = \mathbf{v}^0(x_2)\,. \tag{27}$$

To find the boundary condition on $\boldsymbol{\sigma}^0$ on $\mathbf{\Gamma}_s$, we use the order 0 matching condition on stress and integrate it over the segment Y_w to obtain

$$\lim_{y_1 \to \infty} \int_{Y_w} \boldsymbol{\tau}^0(x_2, y_1, y_2) \cdot \hat{\mathbf{x}}_1 \, dy_2 = \lambda_m \boldsymbol{\sigma}^0(0, x_2) \cdot \hat{\mathbf{x}}_1 \tag{28}$$

Integrating (17) for $i = -1$ on $\mathbb{Y}$ and then, by parts, we find

$$\int_{\partial \mathbb{Y}} \boldsymbol{\tau}^0 \cdot \mathbf{n} \, d\mathbf{y} = \mathbf{0}\,. \tag{29}$$

In the last equation, the integrals over borders $\mathbf{Y}_1$ and $\mathbf{Y}_2$ cancel themselves because of the periodicity in y_2, the one over $\mathbf{\Gamma}$ vanishes because of the free boundary conditions and therefore,

$$\int_{\mathbf{Y}_3} \boldsymbol{\tau}^0 \cdot \hat{\mathbf{x}}_1 \, d\mathbf{y} = \mathbf{0}\,. \tag{30}$$

Combining the last equation with (28), we find the order 0 boundary conditions for the volume problem (the outward normal to $\mathbf{\Gamma}_s$ is $\mathbf{n}_s = -\hat{\mathbf{x}}_1$)

$$\boldsymbol{\sigma}^0(0, x_2) \cdot \mathbf{n}_s = \mathbf{0}\,. \tag{31}$$

2.3.2 Order 1

(17) for $i = -1$ and (18) for $i = 0$ give:

$$\boldsymbol{\nabla}_{\mathbf{y}} \cdot \boldsymbol{\tau}^0 = \mathbf{0}\,, \tag{32}$$

$$\boldsymbol{\tau}^0 = \mathbf{c} : \left(\boldsymbol{\epsilon}_{x_2}(\mathbf{v}^0) + \boldsymbol{\epsilon}_{\mathbf{y}}(\mathbf{v}^1)\right)\,. \tag{33}$$

In order to find a simple form for the solutions to the last equations, we seek for

$$\mathbf{v}^1(x_2, \mathbf{y}) = y_1 \frac{\partial \mathbf{u}^0}{\partial x_1} + \hat{\mathbf{v}}(x_2, \mathbf{y})\,, \tag{34}$$

$$\boldsymbol{\tau}^0(x_2, \mathbf{y}) = \boldsymbol{\sigma}^0(0, x_2) + \hat{\boldsymbol{\tau}}(x_2, \mathbf{y})\,, \tag{35}$$

where $\hat{\mathbf{v}}$ and $\hat{\boldsymbol{\tau}}$ are periodic in y_2. Using the fact that $\boldsymbol{\sigma}^0$ does not depend on $\mathbf{y}$, (32) easily gives us

$$\boldsymbol{\nabla}_{\mathbf{y}} \cdot \hat{\boldsymbol{\tau}} = \mathbf{0}\,. \tag{36}$$

Using (27), we have, on $\mathbf{\Gamma}_s$

$$\boldsymbol{\epsilon}_{\mathbf{y}}\left(y_1 \frac{\partial \mathbf{u}^0}{\partial x_1}\right) + \boldsymbol{\epsilon}_{x_2}(\mathbf{v}^0) = \boldsymbol{\epsilon}_{\mathbf{x}}(\mathbf{u}^0)\,, \tag{37}$$

then, (33), (34) and the last equation, yield

$$\boldsymbol{\tau}^0 = \mathbf{c} : \left(\boldsymbol{\epsilon}_{\mathbf{x}}(\mathbf{u}^0) + \boldsymbol{\epsilon}_{\mathbf{y}}(\hat{\mathbf{v}})\right) , \tag{38}$$

$$= \boldsymbol{\sigma}^0 + \mathbf{c} : \boldsymbol{\epsilon}_{\mathbf{y}}(\hat{\mathbf{v}}) , \tag{39}$$

and therefore, using (35), we find

$$\hat{\boldsymbol{\tau}} = \mathbf{c} : \boldsymbol{\epsilon}_{\mathbf{y}}(\hat{\mathbf{v}}) . \tag{40}$$

Using the boundary condition (19), the order 1 asymptotic problem reduces to the following problem:

$$\hat{\boldsymbol{\tau}} = \mathbf{c} : \boldsymbol{\epsilon}_{\mathbf{y}}(\hat{\mathbf{v}}) \quad \text{in} \quad \mathbb{R} \times \mathbb{Y} , \tag{41}$$

$$\boldsymbol{\nabla}_{\mathbf{y}} \cdot \hat{\boldsymbol{\tau}} = \mathbf{0} \quad \text{in} \quad \mathbb{R} \times \mathbb{Y} , \tag{42}$$

$$\hat{\boldsymbol{\tau}} \cdot \mathbf{n} = -\boldsymbol{\sigma}^0(0, x_2) \cdot \mathbf{n} \quad \text{on} \quad \mathbb{R} \times \boldsymbol{\Gamma} , \tag{43}$$

$$\lim_{y_1 \to \infty} \hat{\boldsymbol{\tau}} \cdot \hat{\mathbf{x}}_1 = \mathbf{0} , \tag{44}$$

$$\hat{\mathbf{v}}(x_2, \mathbf{y}) \quad \text{and} \quad \hat{\boldsymbol{\tau}}(x_2, \mathbf{y}) \quad \text{are } \lambda_m\text{-periodic in} \quad y_2 . \tag{45}$$

Based on the linearity of the last problem with respect to the source term $\boldsymbol{\sigma}^0$, noting that, thanks to the boundary condition (31), the only non zero component of $\boldsymbol{\sigma}^0(0, x_2)$ is σ^0_{22}, we seek for solutions to the last problem under the following form:

$$\hat{\mathbf{v}}(x_2, \mathbf{y}) = \sigma^0_{22}(0, x_2)\mathbf{V}(\mathbf{y}) + \langle \hat{\mathbf{v}} \rangle (x_2) \tag{46}$$

$$\hat{\boldsymbol{\tau}}(x_2, \mathbf{y}) = \sigma^0_{22}(0, x_2)\mathbf{T}(\mathbf{y}) , \tag{47}$$

where $\mathbf{V}$ and $\mathbf{T}$ are periodic in y_2. From equations (41–45), we find that $\mathbf{V}$ and $\mathbf{T}$ are solutions of the following cell problem:

$$\begin{cases} \mathbf{T} = \mathbf{c} : \boldsymbol{\epsilon}_{\mathbf{y}}(\mathbf{V}) \quad \text{in} \quad \mathbb{Y} , \\ \boldsymbol{\nabla}_{\mathbf{y}} \cdot \mathbf{T} = \mathbf{0} \quad \text{in} \quad \mathbb{Y} , \\ \mathbf{T} \cdot \mathbf{n} = -n_2 \, \hat{\mathbf{x}}_2 \quad \text{on} \quad \boldsymbol{\Gamma} , \\ \lim_{y_1 \to \infty} \mathbf{T} \cdot \hat{\mathbf{x}}_1 = \mathbf{0} . \\ \mathbf{T} \quad \text{and} \quad \mathbf{V} \quad \lambda_m\text{-periodic in } y_2. \end{cases} \tag{48}$$

In general, the last problem can only be solved with a numerical solver, like a finite elements solver.

At this stage, we are able to fully compute $\hat{\boldsymbol{\tau}}$ and incompletely $\hat{\mathbf{v}}$ ($\langle \hat{\mathbf{v}} \rangle$ is not determined).

We now need to compute the order 1 boundary condition for the volume problem, $\boldsymbol{\sigma}^1 \cdot \mathbf{n}_s$, on $\boldsymbol{\Gamma}_s$. At this point, we assume the external source $\boldsymbol{f}$ is not in the boundary layer area. If it is not the case, the source is reintroduced after the resolution of the equations with an energy argument as shown in

Sec. 2.4.1. Integrating the stress matching condition (13) for $i=1$ over the Y_w segment, we find

$$\lambda_m \boldsymbol{\sigma}^1(0,x_2) = \lim_{y_1\to\infty}\left(\int_{Y_w}\boldsymbol{\tau}^1(x_2,\mathbf{y})\,dy_2 - y_1\lambda_m\frac{\partial\boldsymbol{\sigma}^0}{\partial x_1}(0,x_2)\right). \tag{49}$$

(17) for $i=0$ gives

$$\boldsymbol{\nabla}_{\mathbf{y}}\cdot\boldsymbol{\tau}^1 = \rho\ddot{\mathbf{v}}^0 - \boldsymbol{\nabla}_{x_2}\cdot\boldsymbol{\tau}^0\,, \tag{50}$$

and therefore, using (35),

$$\boldsymbol{\nabla}_{\mathbf{y}}\cdot\boldsymbol{\tau}^1 + \boldsymbol{\nabla}_{x_2}\cdot\boldsymbol{\sigma}^0(0,x_2) + \boldsymbol{\nabla}_{x_2}\cdot\hat{\boldsymbol{\tau}} = \rho\ddot{\mathbf{v}}^0\,. \tag{51}$$

Using (27), integrating the last equation over $\mathbb{Y}(y_1)$ and passing to the limit, we obtain

$$\boldsymbol{\nabla}_{x_2}\cdot\int_{\mathbb{Y}}\hat{\boldsymbol{\tau}}d\mathbf{y} = \lim_{y_1\to\infty}\left(-\int_{\mathbb{Y}(y_1)}\boldsymbol{\nabla}_{\mathbf{y}}\cdot\boldsymbol{\tau}^1 d\mathbf{y}' + |\mathbb{Y}(y_1)|\left(-\boldsymbol{\nabla}_{x_2}\cdot\boldsymbol{\sigma}^0 + \rho\ddot{\mathbf{u}}^0\right)\right). \tag{52}$$

Using an integration by parts, the free boundary condition along $\boldsymbol{\Gamma}$ and the periodicity in y_2, we find

$$\int_{\mathbb{Y}(y_1)}\left(\boldsymbol{\nabla}_{\mathbf{y}}\cdot\boldsymbol{\tau}^1\right)(x_2,\mathbf{y}')\,d\mathbf{y}' = \int_{\partial\mathbb{Y}(y_1)}\left(\boldsymbol{\tau}^1\cdot\mathbf{n}\right)(x_2,\mathbf{y}')\,d\mathbf{y}' \tag{53}$$

$$= \int_{Y_w}\boldsymbol{\tau}^1(x_2,y_1,y_2)\cdot\hat{\mathbf{x}}_1\,dy_2\,. \tag{54}$$

Combining (49) and (54) in (52), we have

$$\boldsymbol{\nabla}_{x_2}\cdot\left(\int_{\mathbb{Y}}\hat{\boldsymbol{\tau}}d\mathbf{y}\right) = -\lambda_m\boldsymbol{\sigma}^1\cdot\hat{\mathbf{x}}_1 + \lim_{y_1\to\infty}\left(-y_1\lambda_m\frac{\partial\boldsymbol{\sigma}^0}{\partial x_1}\cdot\hat{\mathbf{x}}_1 + |\mathbb{Y}(y_1)|\left(-\boldsymbol{\nabla}_{x_2}\cdot\boldsymbol{\sigma}^0 + \rho\ddot{\mathbf{u}}^0\right)\right). \tag{55}$$

Eq. (14) for $i=0$ yields

$$\frac{\partial\boldsymbol{\sigma}^0}{\partial x_1}\cdot\hat{\mathbf{x}}_1 = -\boldsymbol{\nabla}_{x_2}\cdot\boldsymbol{\sigma}^0 + \rho\ddot{\mathbf{u}}^0\,, \tag{56}$$

which, combined with (55), gives

$$\boldsymbol{\nabla}_{x_2}\cdot\left(\int_{\mathbb{Y}}\hat{\boldsymbol{\tau}}d\mathbf{y}\right) = -\lambda_m\boldsymbol{\sigma}^1\cdot\hat{\mathbf{x}}_1 + \lim_{y_1\to\infty}\left(|\mathbb{Y}(y_1)| - y_1\lambda_m\right)\left(-\boldsymbol{\nabla}_{x_2}\cdot\boldsymbol{\sigma}^0 + \rho\ddot{\mathbf{u}}^0\right). \tag{57}$$

Finally, based on the last equation, the order 1 volume boundary condition on $\boldsymbol{\Gamma}_s$ can be written as

$$\varepsilon\boldsymbol{\sigma}^1(0,x_2)\cdot\hat{\mathbf{x}}_1 = -\mathbf{b}\frac{\partial\sigma^0_{22}}{\partial x_2} + h\left(-\boldsymbol{\nabla}_{x_2}\cdot\boldsymbol{\sigma}^0 + \rho\ddot{\mathbf{u}}^0\right), \tag{58}$$

where

$$\mathbf{b} = \frac{\varepsilon}{\lambda_m}\int_{\mathbb{Y}}\mathbf{T}\cdot\hat{\mathbf{x}}_2\,d\mathbf{y}\,, \tag{59}$$

$$h = \varepsilon\lim_{y_1\to\infty}\frac{|\mathbb{Y}(y_1)| - y_1\lambda_m}{\lambda_m}\,. \tag{60}$$

It can be seen that h is finite and equal to a, the height difference between $\boldsymbol{\Gamma}_s$ and $\boldsymbol{\Gamma}_a$. It can be shown that only $b_2 = \mathbf{b}\cdot\hat{\mathbf{y}}_2$ component is non-zero. Indeed, integrating $\boldsymbol{\nabla}_{\mathbf{y}}\cdot\mathbf{T} = \mathbf{0}$ over $\mathbf{Y}_3(y_1)$ and using

the periodicity in y_2, we find, for any y_1

$$\int_{\mathbf{Y}_3(y_1)} [\boldsymbol{\nabla}_\mathbf{y} \cdot \mathbf{T}]_i \, d\mathbf{y} = \frac{\partial}{\partial y_1} \int_0^{\lambda_m} T_{1i} \, dy_2 = 0 \,. \tag{61}$$

$\int_0^{\lambda_m} T_{1i} \, dy_2$ is therefore constant in y_1, and, using the fact that $\lim_{y_1 \to \infty} T_{i1} = 0$, we find, for any y_1:

$$\int_0^{\lambda_m} T_{1i}(y_1, y_2) \, dy_2 = \int_0^{\lambda_m} T_{i1}(y_1, y_2) \, dy_2 = 0 \,, \tag{62}$$

which allows to conclude that $b_1 = 0$.

Using again the fact that only σ^0_{22} is non zero on $\boldsymbol{\Gamma}_s$, we can rewrite the order 1 boundary condition on $\boldsymbol{\Gamma}_s$ as:

$$\varepsilon \boldsymbol{\sigma}^1(0, x_2) \cdot \mathbf{n}_s = (b_2 + h) \frac{\partial \sigma^0_{22}}{\partial x_2} \hat{\mathbf{x}}_2 - h\rho \ddot{\mathbf{u}}^0 \,. \tag{63}$$

From the last equation, it can be seen that the x_1 position of the effective free surface $\boldsymbol{\Gamma}_s$ can be chosen such that $b_2 + h = 0$ and, in such a case, the order 1 boundary condition reduces to

$$\varepsilon \boldsymbol{\sigma}^1(0, x_2) \cdot \mathbf{n}_s = -h\rho \ddot{\mathbf{u}}^0 \,. \tag{64}$$

2.4 Practical resolution of the effective equations

Practically, we need to use the above results with a classical wave equation solver like SEM. The idea is to use this solver only in $\boldsymbol{\Omega}_s$, which meshing is simple compared to the one of $\boldsymbol{\Omega}^\varepsilon$. To take into account the order 0 and 1 boundary conditions (equations 31 and 64), the different orders are combined together, as it often done in such a case (e.g. Fish & Chen 2004, Capdeville & Marigo 2007, Capdeville & Marigo 2008, Capdeville *et al.* 2010a):

$$\tilde{\mathbf{u}}^{\varepsilon,i}(\mathbf{x}) = \mathbf{u}^0(\mathbf{x}) + \varepsilon \mathbf{u}^1(\mathbf{x}) + ... + \varepsilon^i \mathbf{u}^i(\mathbf{x}) \,, \tag{65}$$

$$\tilde{\boldsymbol{\sigma}}^{\varepsilon,i}(\mathbf{x}) = \boldsymbol{\sigma}^0(\mathbf{x}) + \varepsilon \boldsymbol{\sigma}^1(\mathbf{x}) + ... + \varepsilon^i \boldsymbol{\sigma}^i(\mathbf{x}) \,, \tag{66}$$

and we have

$$\mathbf{u}^\varepsilon(\mathbf{x}) = \tilde{\mathbf{u}}^{\varepsilon,i}(\mathbf{x}) + O(\varepsilon^{i+1}) \,. \tag{67}$$

From (14) and (15), it can be seen that $\tilde{\mathbf{u}}^{\varepsilon,1}$ and $\tilde{\boldsymbol{\sigma}}^{\varepsilon,1}$ are driven by the same wave equation as for the original problem, but the boundary condition on $\boldsymbol{\Gamma}_s$ is different:

$$\tilde{\boldsymbol{\sigma}}^{\varepsilon,1} \cdot \mathbf{n}_s = -h\rho \ddot{\tilde{\mathbf{u}}}^{\varepsilon,1} \quad \text{on} \quad \boldsymbol{\Gamma}_s \,. \tag{68}$$

So, in practice, solving the original problem in $\boldsymbol{\Omega}^\varepsilon$ is replaced by solving the same wave equation problem but in $\boldsymbol{\Omega}_s$ and replacing the free boundary condition on $\boldsymbol{\Gamma}^\varepsilon$ by the dynamic boundary condition

(68), where the h and b_1 coefficients are computed solving the cell problem (48) with an effective interface $\mathbf{\Gamma}_s$ vertical position such that $b_2 + h = 0$.

If a receiver is close to the free surface (within two or three λ_m), the solution can be corrected to the order 1 with:

$$\tilde{\mathbf{v}}^{\varepsilon,1/2}(\mathbf{x}) = \tilde{\mathbf{u}}^{\varepsilon,1}(0,x_2) + x_1 \frac{\partial \tilde{\mathbf{u}}^{\varepsilon,1}}{\partial x_1}(0,x_2) + \varepsilon \mathbf{V}\left(\frac{\mathbf{x}}{\varepsilon}\right) \tilde{\sigma}_{22}^{\varepsilon,1}(0,x_2)\,. \tag{69}$$

or, to the same order, by

$$\tilde{\mathbf{v}}^{\varepsilon,1/2}(\mathbf{x}) = \tilde{\mathbf{u}}^{\varepsilon,1}(\mathbf{x}) + \varepsilon \mathbf{V}\left(\frac{\mathbf{x}}{\varepsilon}\right) \tilde{\sigma}_{22}^{\varepsilon,1}(0,x_2)\,. \tag{70}$$

Note that we have used an half order ("1/2") because it is only a partial order 1 solution as $\langle \tilde{\mathbf{v}} \rangle$ hasn't been computed. Both expressions are valid, but (70) is useful if the receiver is located in $\mathbf{\Omega}_s$, whereas (69) is useful when a receiver is outside of $\mathbf{\Omega}_s$ (but still in $\mathbf{\Omega}^\varepsilon$).

In practice, for the examples presented in the present paper, including for the non-periodic case, the receiver corrector effects are small.

2.4.1 External source in the boundary layer

If the external source $\boldsymbol{f}$ is within two or three λ_m from $\mathbf{\Gamma}^\varepsilon$, a correction might be necessary. To do so, we follow the same argument as the one used in our previous works (Capdeville *et al.*, 2010a; Capdeville *et al.*, 2010b).

For a moment tensor located in $\mathbf{x}_0$, the external force is

$$\boldsymbol{f}(\mathbf{x},t) = g(t)\mathbf{M} \cdot \boldsymbol{\nabla}\delta(\mathbf{x} - \mathbf{x}_0) \tag{71}$$

where $g(t)$ is the source time wavelet and $\mathbf{M}$ the symmetric moment tensor. As shown by Capdeville *et al.* (2010a), to ensure the conservation of the energy released by the source in the original model, we need to find a moment tensor $\mathbf{M}^{\varepsilon,0}$ such that

$$(\mathbf{u}^\varepsilon, \boldsymbol{f}) = \left(\tilde{\mathbf{u}}^{\varepsilon,0}, \boldsymbol{f}^{\varepsilon,0}\right) + O(\varepsilon)\,, \tag{72}$$

where $(\ .\ ,\ .\ )$ is the L^2 inner product and

$$\boldsymbol{f}^{\varepsilon,0}(\mathbf{x},t) = g(t)\mathbf{M}^{\varepsilon,0} \cdot \boldsymbol{\nabla}\delta(\mathbf{x} - \mathbf{x}_0)\,. \tag{73}$$

Using an integration by parts and the symmetry of the moment tensor, (72) becomes

$$\mathbf{M} : \boldsymbol{\epsilon}\left(\mathbf{u}^\varepsilon\right)|_{\mathbf{x}_0} = \mathbf{M}^{\varepsilon,0} : \boldsymbol{\epsilon}_x\left(\tilde{\mathbf{u}}^{\varepsilon,0}\right)|_{\mathbf{x}_0} + O(\varepsilon)\,. \tag{74}$$

Using (11), expansion (9) and property (37), after some calculus, we find, to the order 0

$$\mathbf{M}^{\varepsilon,0} = \mathbf{G}^\varepsilon(\mathbf{x}_0/\varepsilon) : \mathbf{M}\,, \tag{75}$$

where

$$G^{\varepsilon}_{ijkl}(\mathbf{y}) = \frac{1}{2}\left(\delta_{ik}\delta_{jl} + \delta_{jk}\delta_{il}\right) + c_{ij22}\epsilon_{\mathbf{y},kl}\left(\mathbf{V}\right)\left(\mathbf{y}\right) \tag{76}$$

2.5 Numerical considerations

2.5.1 Numerical resolution of the cell problem

In general, solving the cell problem (48) cannot be done analytically and a finite element solver is required. The periodic cell $\mathbb{Y}$ is not bounded in y_1 which could be a problem. Practically it is not: the solution $\mathbf{T}$ exponentially decays to zero (Sanchez-Palencia, 1986; Dumontet, 1990), and therefore, a bounded $\mathbb{Y}$ with the $\mathbf{Y}_3$ boundary placed at a depth of $3\lambda_m$ with a free boundary condition at the bottom, is enough to obtain a good solution. We use the same solver as the one developed for the volume homogenization (Capdeville *et al.*, 2010b), a relatively high order finite element method based on a triangular mesh to solve the weak (or variational) form of the cell problem equations. The finite element interpolation is based on the Fekete points (Pasquetti & Rapetti, 2004; Mercerat *et al.*, 2006) and we employ an high order integration quadrature (Rathod *et al.*, 2004). Depending on the shape of the topography, the solutions can present singularities for topography kinks of angle (measured on the solid side) greater than 180° (Grisvard, 1985). These singularities are not a problem for the accuracy of the $\mathbf{b}$ coefficient, nevertheless, it can alter the accuracy of the correctors $\mathbf{V}$ and $\mathbf{T}$, which means that these singularities may need some attentions (by using locally a denser mesh, for example) if a source or a receiver are in the vicinity of such a singularity. Once (48) solved, the b_2 and h coefficients can easily be computed and the $\mathbf{\Gamma}_s$ vertical position such that $b_2 + h = 0$ yields.

2.5.2 Numerical resolution of the effective wave equation

For the wave equation solver, we use a spectral element tool. To implement the order 1 boundary correction (63), we need to modify the internal forces and the mass matrix. If the effective topography $\mathbf{\Gamma}_s$ is chosen such that h is positive (that is $\mathbf{\Gamma}_s$ is below the average topography $\mathbf{\Gamma}_a$), then the mass matrix modification always leads to a stable scheme. The internal forces modification on the other hand often leads to an unstable scheme. Choosing $\mathbf{\Gamma}_s$ vertical position such that $h = -b_2$ solves the problem: in such a case, as already mentioned at the end of Sec. 2.3, the internal forces modification is zero and therefore always stable. Furthermore, we will see that b_2 is always negative, which leads to a positive h and close to be equal to half of the average height of the interface topography amplitude variation $e/2$. With such a choice, we see that the wave somehow propagates below the fast topography, and that only the inertial effect of the topography affects the wave.

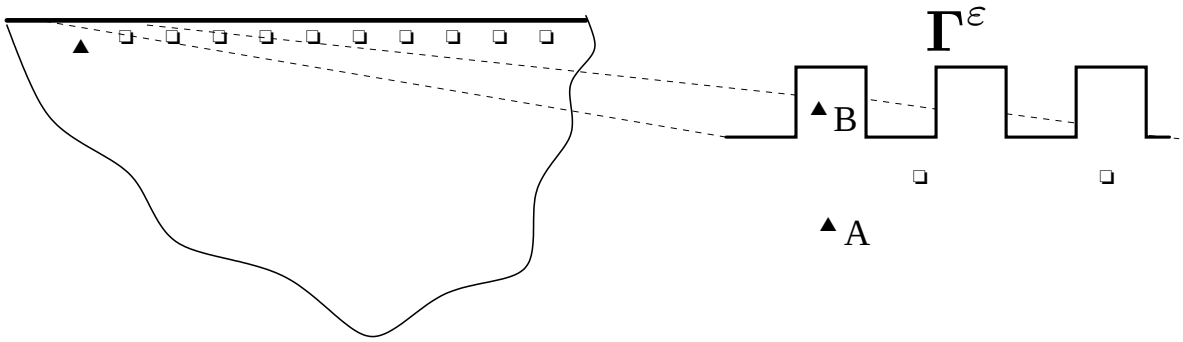

Figure 3. Configuration for the periodic test. The white squares represent the receiver locations and the triangle A and B the two source locations used for the tests.

ε	0.2	0.1	0.05
e	100 m	50 m	25 m
b_2	-46.4 m	-23.2 m	-11.6 m
error order 0	1.2	1.3	1.1
error order 1	1.2	0.27	0.05

Table 1. Values of computed b_2 and $E(\tilde{\mathbf{u}}^{0,\varepsilon})$ and $E(\tilde{\mathbf{u}}^{1,\varepsilon})$ L_2 norm error (see (77)) for 3 values of ε.

2.6 Validation tests

We carry out a validation test in a simple configuration presented on Fig. 3. The actual domain size is 80×20 km^2 surrounded wih a Perfectly Matched Layer (PML, in the version proposed by Festa *et al.* (2005)), but for the top. The source is either located 200 m below the free surface (triangle A on Fig. 3) or in the topography (triangle B on Fig. 3). The receivers are located 100 m below the free surface (white squares on Fig. 3). The density, S wave velocity and P wave velocity are, respectively, 3000 kg/m^3, 3.2 km/s and 5 km/s. The source time wavelet is a Ricker (second derivative of a Gaussian). Its maximum frequency is 3.2 H_z, such that the minimum wavelength λ_m is about 1 km. Three values of ε are tested, 0.2, 0.1 and 0.05, corresponding respectively to e =100 m, 50 m and 25 m and l =200 m, 100 m and 50 m. A reference solution is computed for the three cases with a SEM mesh based on degree 5 elements. Knowing that, for an homogeneous body, 1 km width elements would be enough for an accurate result, for ε =0.05 the mesh is oversampling the wavefield by a factor 40, leading to an over-cost of a factor 1600 for a structured mesh. For the asymptotic solution, we use a flat interface $\mathbf{\Gamma}_s$ location such that $b_2 + h = 0$. Solving the cell problem, the obtained values for b_2 are given in Tab. 1. It is interesting to note that, in each case, b_2 has a value close to $e/2$. This means that the effective interface $\mathbf{\Gamma}_s$ is almost located at the bottom of the interface topography. For

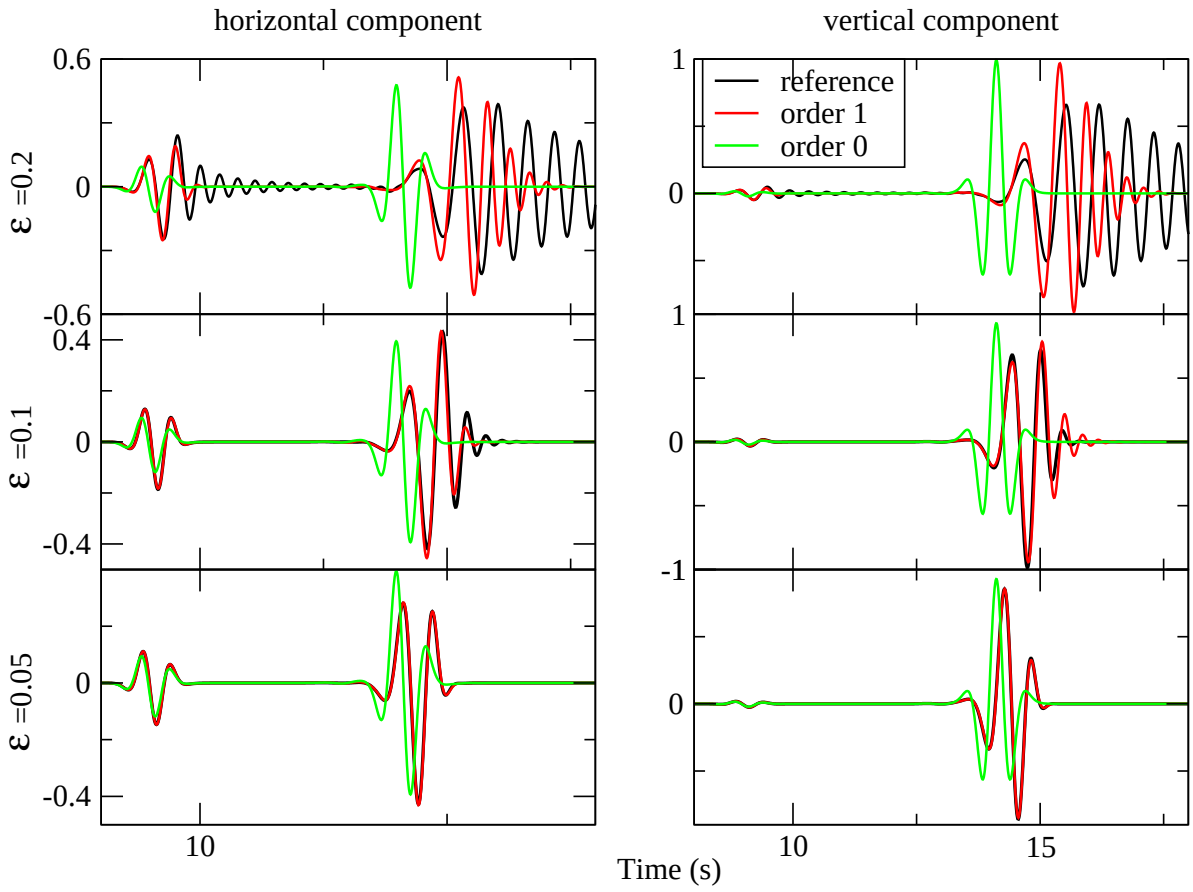

Figure 4. Vertical (right graphs) and horizontal components (left graphs) for the reference solution (black line), order 0 solution (green line) and order 1 solution (red line) for three values of ε (ε =0.2 top graphs, ε =0.1 middle graphs, ε =0.05 bottom graphs) and for an epicentral distance of 35 km.

the order 0 solution, we just perform regular spectral element simulations in $\mathbf{\Omega}_s$ for each value of ε ($\mathbf{\Omega}_s$ changes for each ε value because $\mathbf{\Gamma}_s$ changes with ε). For the order 1, we perform the same spectral element simulations as for the order 0, but this time taking into account the order 1 boundary condition (that is just an extra weight). A sample of the obtained seismograms for both components is presented on Fig. 4 for a receiver located 35 km away from the source. It can be seen that the order 0 solution is not accurate, even for such small values of ε. To more precisely investigate the accuracy of the method, we use the following L_2 norm error:

$$E(\mathbf{u}) = \frac{1}{N}\sum_{i=1}^{N} \frac{\sqrt{\int_0^{t_{max}} (\dot{\mathbf{u}} - \dot{\mathbf{u}}^{ref})^2(\mathbf{x}_i,t)dt}}{\sqrt{\int_0^{t_{max}} \left(\dot{\mathbf{u}}^{ref}\right)^2(\mathbf{x}_i,t)dt}}, \tag{77}$$

where N is the number of receivers. For the order 0, even if no convergence for the L_2 norm is observed in the presented range of ε (see Tab. 1), it can be seen, observing the traces on Fig. 4, that the phase is roughly getting better in ε and we can therefore guess that, at some point, for very small ε, a

L_2 error convergence in ε would be observed. For the order 1, first, the accuracy of the results, is much better than for the order 0 for all the tested values of ε, and second, the convergence is roughly in ε^2 between $\varepsilon = 0.2$ and 0.1 (see Tab. 1). The inertial effect of the order 1 boundary condition is therefore important and we can conclude by a physical interpretation: the elastic waves are not propagating in the fast topography, but they are propagating below it and the fast topography is just acting as a incompressible infinitely thin layer of material loading the free surface. As expected, the extra weight due to the fast topography is slowing down the apparent velocity of the surface wave.

We haven't shown any seismograms computed using the average topography $\mathbf{\Gamma}_a$ as an effective topography, which is the solution commonly adopted. This is because they are very similar to the one obtained using $\mathbf{\Gamma}_s$, just a small amplitude difference would be seen.

Finally a test for a source within the boundary layer (triangle B on Fig. 3) is performed. On Fig. 5 are shown the vertical component seismograms for an epicentral distance of 35 km for three cases: order 1 without the source correction (75), the order 1 with the source correction (75) and, for comparison, the order 0 with the source correction (75). It can be noted that the amplitude of the signal without the source correction is way too large compared to the reference seismogram, and once corrected, the signal amplitudes have a good match. For a more accurate result, a smaller ε would be required. Finally, let us mention that obtaining the reference with SEM is not trivial in such a case. Indeed, the mesh has needed to be designed far finer than the usual sampling of the wavefield to converge, leading to an impressive numerical over-cost. This is unusual because even for highly inhomogeneous medium, no serious oversampling around the source is most of the time required. For a source embedded within a fast topography, this is different and a serious oversampling has been necessary to obtain a converged solution. This shows how useful can be the present asymptotic method in such case (the mesh for the effective solution does not need any oversampling, even around the source).

3 NON-PERIODIC CASE

In this section, the boundary variations are not assumed to be periodic anymore. We consider a general deterministic boundary $\mathbf{\Gamma}^0$ on the top of our infinite half space $\mathbf{\Omega}^0$. We seek for an approximate solution to the displacement $\mathbf{u}^{ref}$ solution of the wave equation:

$$\begin{aligned} \rho\partial_{tt}\mathbf{u}^{ref} - \boldsymbol{\nabla}\cdot\boldsymbol{\sigma}^{ref} &= \boldsymbol{f} \quad \text{in } \mathbf{\Omega}^0\,, \\ \boldsymbol{\sigma}^{ref} &= \mathbf{c} : \boldsymbol{\epsilon}(\mathbf{u}^{ref}) \quad \text{in } \mathbf{\Omega}^0\,, \\ \boldsymbol{\sigma}^{ref}\cdot\mathbf{n} &= \mathbf{0} \quad \text{on } \mathbf{\Gamma}^0\,, \end{aligned} \tag{78}$$

where $\mathbf{n}$ is the outward normal to $\mathbf{\Gamma}^0$.

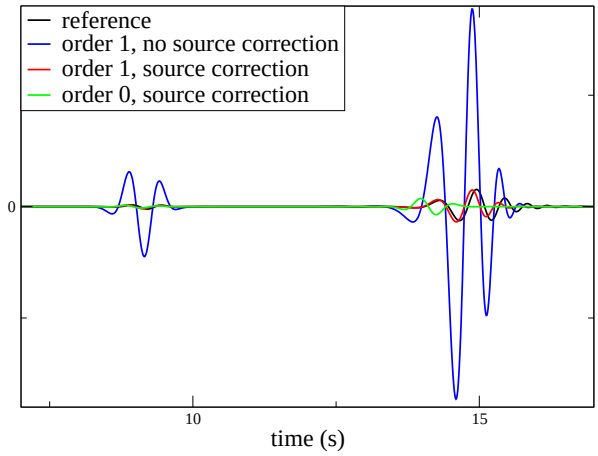

Figure 5. Horizontal component seismograms for the source within the boundary layer (triangle B on Fig. 3) for a receiver 35 km away from the source. The reference solution (black line), the order 1 solution without the source correction (75) (blue line) the order 1 with the source correction (75) (red line) and order 0 solution with the source correction (red line) for values of $\varepsilon = 0.1$ are plotted.

Before we start, let us summarize the ideas of the following development. For the non periodic case, the periodicity is not there anymore to allow to separate naturally the microscopic from the macroscopic scales and to build a series of problem depending on a small parameter ε. The main idea of the non-periodic homogenization is to introduce manually a scale separation. To do so, the Fourier domain in the "horizontal direction" is used and a user defined wave number k_0 is set to be the limit between the slow variations ($k < k_0$) and the fast ones ($k > k_0$). The k_0 allows to define a small parameter $\varepsilon_0 = 1/(k_0\lambda_m)$. The "horizontal direction" mentioned above needs to be precised: the effective surface waves are propagating along an effective free surface that is not necessarily flat and the "horizontal direction" means here "along the effective topography". Following this idea, we build the microscopic variable $\mathbf{y} = \boldsymbol{\zeta}_{\varepsilon_0}^{-1}(\mathbf{x})/\varepsilon$ where $\boldsymbol{\zeta}_{\varepsilon_0}$ is a transformation built such that the effective topography is the image of the flat y_2 axis. Therefore, in the $\mathbf{y}$ domain, the effective topography is flat. ε is a small parameter meant to play the same role as the ε of the periodic case is introduced. It is in general different from ε_0. Once ε_0 is set and fixed, the fast variable $\mathbf{y}$ defined, a series of two scale topography $\boldsymbol{\Gamma}^{\varepsilon_0,\varepsilon}$ is built, leading to a series of ε-indexed series of problem. This series of problem is equal to the original problem only when $\varepsilon_0 = \varepsilon$ and when $\mathbf{x} = \boldsymbol{\zeta}_{\varepsilon_0}(\varepsilon_0\mathbf{y})$. Once the construction of the series of problem is done, even if some complications due to the transformation $\boldsymbol{\zeta}_{\varepsilon_0}$ appear, the resolution of the homogenization problem is essentially the same as for the periodic case as well as the form of the solution up to the order 1. As for the periodic case, we find that the leading term of the asymptotic solution $\mathbf{u}^{\varepsilon_0,0}$ does not depend upon ε but depends on ε_0. In other words, for each fixed value of ε_0, we have a two scale homogenization problem leading to particular homogenized solution

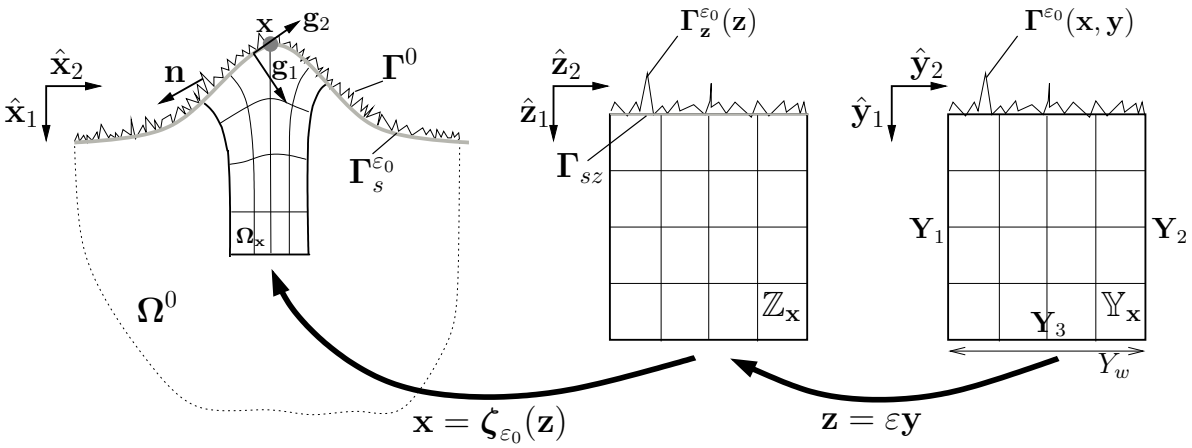

Figure 6. The non-periodic domains and transformation

and therefore the homogenized solution depends on the initial choice of the k_0 in the Fourier domain. Once the two scale problem is solved, the effective topography still needs to be found. Indeed, we have so far assumed that the effective topography is known, which is not the case at the initial stage. The solution adopted here is iterative and based on the following criteria: a smooth topography is thought to be the effective topography if the fast variable part ($\mathbf{y}$ part) of the the correctors, solutions to the cell problem ($\mathbf{T}$ and $\mathbf{V}$), computed with such an effective topography, present only fast variations in the horizontal direction, i.e. their Fourier spectrum is zero for $k < k_0$ in the $\mathbf{y}$ domain.

3.1 Settings

For the non-periodic case, the small parameter ε is not as clearly defined as for the periodic case:

$$\varepsilon = \frac{\lambda}{\lambda_m}\,, \tag{79}$$

where λ is a spatial wavelength or a scale. In the non-periodic case, another parameter is required

$$\varepsilon_0 = \frac{\lambda_0}{\lambda_m}\,, \tag{80}$$

where $\lambda_0 = 1/k_0$ is the user-defined scale below which a wavelength is considered as belonging to the small scale (microscopic) domain. Reciprocally, a wavelength larger than λ_0 is considered as belonging to the large scale (macroscopic) domain. The parameter λ_0 is user-defined, but it makes sense to assume that the wavefield interacts with scales smaller than λ_m. Therefore, choosing an $\varepsilon_0 \ll 1$, which means considering as microscopic boundary topography scales whose size is much smaller than the minimum wavelength, is probably a good guess. ε is a once again purely formal parameter which value has a physical meaning only when $\varepsilon = \varepsilon_0$. We need to define a way to separate scales and we cannot count on a periodicity for this anymore. To this end, we introduce a procedure summarized on Fig. 6. We first assume that we are able to build a smooth "effective" interface $\boldsymbol{\Gamma}_s^{\varepsilon_0}$,

where its quality of being "effective" will be precised later in the paper. $\mathbf{\Gamma}_s^{\varepsilon_0}$ depends upon the ε_0 in a way that will also be precised later on, but ε_0 somehow gives the degree of smoothness of $\mathbf{\Gamma}_s^{\varepsilon_0}$ (the largest is ε_0, the smoothest is $\mathbf{\Gamma}_s^{\varepsilon_0}$). Once again, for the sake of simplicity and without loosing the generality of the results, we assume that $\mathbf{\Gamma}_s^{\varepsilon_0}$ can be written as $\mathbf{\Gamma}_s^{\varepsilon_0} = \{\mathbf{x} \in \mathbb{R}^2; x_1 = \Gamma_s^{\varepsilon_0}(x_2)\}$. We define $\mathbf{\Omega}_s^{\varepsilon_0}$, the part of $\mathbb{R}^2$ below $\mathbf{\Gamma}_s^{\varepsilon_0}$ ($\mathbf{\Omega}_s^{\varepsilon_0} = \{\mathbf{x} \in \mathbb{R}^2; x_1 \geq \Gamma_s^{\varepsilon_0}(x_2)\}$) . For a given $\mathbf{x}$ belonging to $\mathbf{\Gamma}_s^{\varepsilon_0}$, we define $\mathbf{\Omega}_\mathbf{x}$, a sub-domain of $\mathbf{\Omega}^0$ centered around $\mathbf{x}$ (see Fig. 6). We define the transformation $\mathbf{x} = \boldsymbol{\zeta}_{\varepsilon_0}(\mathbf{z})$, from $\mathbb{Z}_\mathbf{x}$ to $\mathbf{\Omega}_\mathbf{x}$ (see Fig. 6), such that $\mathbf{\Gamma}_s^{\varepsilon_0} = \boldsymbol{\zeta}_{\varepsilon_0}(\mathbf{\Gamma}_{sz})$, where $\mathbf{\Gamma}_{sz} = \{\mathbf{z} \in \mathbb{Z}_\mathbf{x} \ ; \ z_1 = 0\}$ and such that $\mathbb{Z}_\mathbf{z}$ sides are along $z_2 = constante$ lines. $\mathbb{Z}_\mathbf{z}$ is a rectangular domain with the rough topography $\mathbf{\Gamma}_\mathbf{z}^{\varepsilon_0}$ on the top, where $\mathbf{\Gamma}_\mathbf{z}^{\varepsilon_0}$ is such that $\mathbf{\Gamma}^0 = \boldsymbol{\zeta}_{\varepsilon_0}(\mathbf{\Gamma}_\mathbf{z}^{\varepsilon_0})$.

The $\mathbf{x}$ dependency of $\mathbb{Z}_\mathbf{x}$ needs to be discussed. If in general, one transformation $\boldsymbol{\zeta}_{\varepsilon_0}$ per $\mathbf{x}$ may be required, in 2D it is possible to define a single transformation for all $\mathbf{x}$, or at least a piecewise transformation for different topography segments. Consequently, the $\mathbb{Z}$ can be considered as independent of $\mathbf{x}$.

The transformation $\boldsymbol{\zeta}_{\varepsilon_0}$ defines a curvilinear coordinate system such that a position vector $\mathbf{x}$ in $\mathbf{\Omega}_\mathbf{x}$ can be written as:

$$\mathbf{x} = x_i \hat{\mathbf{x}}_i = z^\alpha \mathbf{g}_\alpha \,, \tag{81}$$

where $\mathbf{x} = \boldsymbol{\zeta}_{\varepsilon_0}(\mathbf{z})$ and

$$\mathbf{g}_\alpha = \frac{\partial \left[\boldsymbol{\zeta}_{\varepsilon_0}\right]_i}{\partial z^\alpha} \hat{\mathbf{x}}_i \tag{82}$$

is the covariant basis vectors and z^α the contravariant components. Note that the $\mathbf{g}_\alpha$ vectors depend on ε_0. We also define the $\mathbb{Z}$ normalized covariant basis vector

$$\hat{\mathbf{z}}_i = \hat{\mathbf{g}}_i = \frac{\mathbf{g}_i}{\sqrt{g_{ii}}} \quad \text{(no sum)} \quad , \tag{83}$$

where g_{ij} is the metric tensor of the curvilinear coordinate system. Furthermore, we assume that in the neighborhood of $\mathbf{\Gamma}_s^{\varepsilon_0}$, this curvilinear coordinate system is locally orthogonal, such that

$$\mathbf{g}_i \cdot \mathbf{g}_j = g_{ii}\delta_{ij} \quad \text{(no sum) for } \mathbf{z} \text{ close to } \mathbf{\Gamma}_{sz} \quad . \tag{84}$$

Thanks to this orthogonality of the curvilinear coordinate system in the neighborhood of the effective interface, we can assume that outward normal $\mathbf{n}$ to $\mathbf{\Gamma}^0$ is also normal to $\mathbf{\Gamma}_z^{\varepsilon_0}$, the top boundary of $\mathbb{Z}$. For the sake of simplicity, we also assume that no length deformation occurs in the the neighborhood of the effective interface with the transformation $\boldsymbol{\zeta}_{\varepsilon_0}$ and therefore $\mathbf{g}_i \cdot \mathbf{g}_j = \delta_{ij}$ (the metric tensor is the identity). This last assumption is not really necessary, but it avoids to have to take the metric tensor into account in the following development, especially for the spatial filtering operations. With such an

assumption, we simply have

$$\hat{\mathbf{z}}_i = \hat{\mathbf{g}}_i = \mathbf{g}_i \,, \tag{85}$$

and the $\hat{\mathbf{z}}_i$ basis vectors are orthonormal.

We once again define the fast variable $\mathbf{y}$, but this time with respect to $\mathbf{z}$:

$$\mathbf{y} = \frac{\mathbf{z}}{\varepsilon} \,, \tag{86}$$

and therefore

$$\mathbf{y} = \frac{\boldsymbol{\zeta}_{\varepsilon_0}^{-1}(\mathbf{x})}{\varepsilon} \,. \tag{87}$$

$\mathbf{y}$ takes values in $\mathbb{Y}$ which unit basis vectors $\hat{\mathbf{y}}_i$ are the same as $\hat{\mathbf{z}}_i$. Note that the unit vectors $\hat{\mathbf{y}}_i$ do not depend upon $\mathbf{y}$, nevertheless, they depend upon $\mathbf{x}$. $\mathbb{Z}_{\mathbf{x}}$ is the image of $\mathbb{Y}_{\mathbf{x}}$ through the transformation (86). The domain $\mathbb{Y}_{\mathbf{x}}$ in general, depends upon $\mathbf{x}$, nevertheless, as mentioned earlier, we can define a single transformation $\boldsymbol{\zeta}_{\varepsilon_0}$ for the whole domain $\boldsymbol{\Omega}^0$ which allows to drop the $\mathbb{Y}$ dependency on $\mathbf{x}$.

When $\varepsilon \to 0$, we consider $\mathbf{z}$ and $\mathbf{y}$ (and therefore $\mathbf{x}$ and $\mathbf{y}$) as independent variables.

Similarly to the periodic case, this $\mathbf{x}$ and $\mathbf{y}$ independence implies that partial derivatives with respect to $\mathbf{x}$ become

$$\boldsymbol{\nabla}_{\mathbf{x}} \to \boldsymbol{\nabla}_{\mathbf{x}} + \frac{1}{\varepsilon}\boldsymbol{\nabla}_{\mathbf{y}} \,, \tag{88}$$

and

$$\boldsymbol{\epsilon}_{\mathbf{x}} \to \boldsymbol{\epsilon}_{\mathbf{x}} + \frac{1}{\varepsilon}\boldsymbol{\epsilon}_{\mathbf{y}} \,, \tag{89}$$

where it is necessary to detail the action of $\boldsymbol{\nabla}_{\mathbf{y}}$. The $\mathbf{y}$ divergence of a second rank tensor $\mathbf{d}$ is

$$\boldsymbol{\nabla}_{\mathbf{y}} \cdot \mathbf{d} = \frac{\partial d^{\alpha\beta}}{\partial y_\alpha}\hat{\mathbf{y}}_\beta \,, \tag{90}$$

where $d^{\alpha\beta}$ are the contravariant components of $\mathbf{d}$ in the curvilinear coordinate system. Similarly, for any vector $\mathbf{h}$,

$$\boldsymbol{\epsilon}_{\mathbf{y}}(\mathbf{h}) = \frac{1}{2}\left(\frac{\partial h^\alpha}{\partial y_\beta} + \frac{\partial h^\beta}{\partial y_\alpha}\right)\, \hat{\mathbf{y}}_\alpha \otimes \hat{\mathbf{y}}_\beta \,, \tag{91}$$

where $\otimes$ is the tensor product. Note that no partial derivative of the $\mathbf{g}_\alpha$ basis vector are involved as it would be the case for a $\mathbf{x}$ divergence or gradient expressed in the curvilinear coordinate system. For example, the contravariant component of the $\mathbf{x}$ divergence of $\mathbf{d}$ is

$$[\boldsymbol{\nabla}_{\mathbf{x}} \cdot \mathbf{d}]^\alpha = \frac{\partial d^{\alpha\beta}}{\partial z^\alpha} + C^\alpha_{\alpha\gamma}\, d^{\gamma\beta} + C^\beta_{\alpha\gamma}\, d^{\alpha\gamma} \,, \tag{92}$$

where $C^\gamma_{\alpha\beta}$ are the Cristoffel symbols of the second kind and $[\cdot]^\alpha$ the α contravariant component.

We define the wavelet $w_m(y_2) = w_{k_m}(y_2)$ where w_{k_m} is the lowpass filter wavelet with a

wavenumber cutoff around $k_m = 1/\lambda_m$. We assume that the support of w_m is contained in $[-\alpha\lambda_m, +\alpha\lambda_m]$ where α is a positive number that depends upon the specific design of w. We assume that the transformation $\boldsymbol{\zeta}_{\varepsilon_0}$ is such the width of the periodic cell $Y_w = [0, 2\beta\lambda_m]$ where β is a positive number greater than α. We also define, $\mathbb{Y}_{\mathbf{z}}$ a boxcar limited version of $\mathbb{Y}$ centered on $\mathbf{z}$:

$$\mathbb{Y}_{\mathbf{z}} = \{\mathbf{y} \in \mathbb{Y}; y_2 \in [\varepsilon z_2 - \beta\lambda_m, \varepsilon z_2 + \beta\lambda_m]\} \,. \tag{93}$$

We define $\boldsymbol{\mathcal{T}} = \{\mathbf{t}(z_2, \mathbf{y}) : \mathbb{R} \times \mathbb{Y}_{\mathbf{z}} \to \mathbb{R}\,, Y_w\text{-periodic in } y_2\}$ the set of functions or tensors defined in $\mathbf{y}$ on $\mathbb{Y}_{\mathbf{z}}$ and periodically extended to $\mathbb{R}$ in y_2. We define the lowpass filtering operator, for any tensor of function $\mathbf{t} \in \boldsymbol{\mathcal{T}}$:

$$\mathcal{F}(\mathbf{t})(z_2, \mathbf{y}) = \int_{\mathbb{R}} \mathbf{t}(z_2, y_1, y_2') w_m(y_2 - y_2') dy_2' \,. \tag{94}$$

$\mathcal{F}(\mathbf{t})$ is a lowpass filtered version of $\mathbf{t}$, but only the horizontal (y_2) direction. Finally let $\boldsymbol{\mathcal{V}}$ be the set of tensors of functions $\mathbf{t}(z_2, \mathbf{y})$ such that, for a given z_2, the y_2 part of h is periodic and contains only spatial frequencies higher than k_m, plus a constant value in y_2:

$$\boldsymbol{\mathcal{V}} = \{\mathbf{t} \in \boldsymbol{\mathcal{T}}; \mathcal{F}(\mathbf{t})(z_2, y_1, y_2) = \ll \mathbf{t} \gg (z_2, y_1) \quad \text{for } y_1 > 0 \quad \}\,, \tag{95}$$

where

$$\ll \mathbf{t} \gg (z_2, y_1) = \frac{1}{|Y_w|} \int_{Y_w} \mathbf{t}(z_2, y_1, y_2) dy_2 \,, \tag{96}$$

where $|Y_w| = 2\beta\lambda_m$. In other words, $\boldsymbol{\mathcal{V}}$ is the set of functions that vary rapidly in y_2 and, as mentioned at the beginning of the non-periodic case section, whose Fourier spectra along z_2 is zero for $k < k_0$ plus a constant value. It is the equivalent of the set of y_2 periodic function in the periodic case.

To build the asymptotic problem, we first define a topography $\boldsymbol{\Gamma}^{\varepsilon_0} = \{(\mathbf{x}, \mathbf{y}) \in \mathbb{R}^4; \boldsymbol{\Gamma}_f^{\varepsilon_0}(\mathbf{x}, \mathbf{y}) = 0\}$ with $\boldsymbol{\Gamma}_f^{\varepsilon_0}$ Y_w-periodic in y_2 and such that $\boldsymbol{\Gamma}^{\varepsilon_0}$ and $\boldsymbol{\Gamma}^0$ are the same along $\mathbf{y} = \frac{\boldsymbol{\zeta}_{\varepsilon_0}^{-1}(\mathbf{x})}{\varepsilon_0}$. If we define $\mathbf{P}^{\varepsilon_0,\varepsilon}$ the subspace of $\mathbb{R}^4$ of physical possibilities,

$$\mathbf{P}^{\varepsilon_0,\varepsilon} = \left\{ (\mathbf{x}, \mathbf{y}) \in \mathbb{R}^4; \mathbf{y} = \frac{\boldsymbol{\zeta}_{\varepsilon_0}^{-1}(\mathbf{x})}{\varepsilon} \right\} \tag{97}$$

then this condition can be written as

$$\boldsymbol{\Gamma}^{\varepsilon_0} \cap \mathbf{P}^{\varepsilon_0,\varepsilon_0} = \boldsymbol{\Gamma}^0 \,. \tag{98}$$

We assume that, with such a definition, we can find a smooth effective topography $\boldsymbol{\Gamma}_s^{\varepsilon_0}$ (on which depends $\boldsymbol{\zeta}_{\varepsilon_0}$) such that a solution to the problem described below exists. This assumption is by far not obvious and the construction of such a $\boldsymbol{\Gamma}_s^{\varepsilon_0}$ from $\boldsymbol{\Gamma}^0$, which is a critical point of this article, is left for Sec. 3.4. We define $\boldsymbol{\Gamma}^{\varepsilon_0,\varepsilon}$, a sequence of ε-indexed topography in $\mathbb{R}^2$,

$$\boldsymbol{\Gamma}^{\varepsilon_0,\varepsilon} \equiv \boldsymbol{\Gamma}^{\varepsilon_0} \cap \mathbf{P}^{\varepsilon_0,\varepsilon} \tag{99}$$

leading to a ε-indexed set of wave equation problems

$$\begin{aligned}\rho\partial_{tt}\mathbf{u}^{\varepsilon_0,\varepsilon} - \boldsymbol{\nabla}\cdot\boldsymbol{\sigma}^{\varepsilon_0,\varepsilon} &= \boldsymbol{f} \quad \text{in} \quad \boldsymbol{\Omega}^{\varepsilon_0,\varepsilon}\,,\\ \boldsymbol{\sigma}^{\varepsilon_0,\varepsilon} &= \mathbf{c}:\boldsymbol{\epsilon}(\mathbf{u}^{\varepsilon_0,\varepsilon}) \quad \text{in} \quad \boldsymbol{\Omega}^{\varepsilon_0,\varepsilon}\,,\\ \boldsymbol{\sigma}^{\varepsilon_0,\varepsilon}\cdot\mathbf{n}^{\varepsilon_0,\varepsilon} &= \mathbf{0} \quad \text{on} \quad \boldsymbol{\Gamma}^{\varepsilon_0,\varepsilon}\,,\end{aligned} \tag{100}$$

where $\boldsymbol{\Omega}^{\varepsilon_0,\varepsilon}$ is the half space below $\boldsymbol{\Gamma}^{\varepsilon_0,\varepsilon}$ and $\mathbf{n}^{\varepsilon_0,\varepsilon}$ its outward normal. This ε-indexed set of problems is purely formal and designed to set up an asymptotic problem for which most of the properties obtained for the periodic case are still valid. It is the equivalent of the problem (3) for the periodic case. Its solutions $\mathbf{u}^{\varepsilon_0,\varepsilon}$ can be related to the solution of the original problem only when $\varepsilon_0 = \varepsilon$ as discussed in Sec. 3.5.

We still consider two asymptotic expansions for the solutions $(\mathbf{u}^{\varepsilon_0,\varepsilon}, \boldsymbol{\sigma}^{\varepsilon_0,\varepsilon})$,

- one valid **away from $\boldsymbol{\Gamma}^{\varepsilon_0,\varepsilon}$, $\mathbf{x}\in\boldsymbol{\Omega}_s^{\varepsilon_0}$:**

$$\mathbf{u}^{\varepsilon_0,\varepsilon}(\mathbf{x}) = \mathbf{u}^{\varepsilon_0,0}(\mathbf{x}) + \varepsilon\mathbf{u}^{\varepsilon_0,1}(\mathbf{x}) + \varepsilon^2\mathbf{u}^{\varepsilon_0,2}(\mathbf{x}) + ... \tag{101}$$

$$\boldsymbol{\sigma}^{\varepsilon_0,\varepsilon}(\mathbf{x}) = \boldsymbol{\sigma}^{\varepsilon_0,0}(\mathbf{x}) + \varepsilon\boldsymbol{\sigma}^{\varepsilon_0,1}(\mathbf{x}) + \varepsilon^2\boldsymbol{\sigma}^{\varepsilon_0,2}(\mathbf{x}) + ... \tag{102}$$

- one valid **close to $\boldsymbol{\Gamma}^{\varepsilon_0,\varepsilon}$**, for $(z_2,\mathbf{y})\in\mathbb{R}\times\mathbb{Y}_{\mathbf{z}}$,

$$\mathbf{u}^{\varepsilon_0,\varepsilon}(\mathbf{x}) = \mathbf{v}^{\varepsilon_0,0}(z_2,\mathbf{y}) + \varepsilon\mathbf{v}^{\varepsilon_0,1}(z_2,\mathbf{y}) + \varepsilon^2\mathbf{v}^{\varepsilon_0,2}(z_2,\mathbf{y}) + ... \tag{103}$$

$$\boldsymbol{\sigma}^{\varepsilon_0,\varepsilon}(\mathbf{x}) = \frac{1}{\varepsilon}\boldsymbol{\tau}^{\varepsilon_0,-1}(z_2,\mathbf{y}) + \boldsymbol{\tau}^{\varepsilon_0,0}(z_2,\mathbf{y}) + \varepsilon\boldsymbol{\tau}^{\varepsilon_0,1}(z_2,\mathbf{y}) + \varepsilon^2\boldsymbol{\tau}^{\varepsilon_0,2}(z_2,\mathbf{y}) + ... \tag{104}$$

where the loose notation $\mathbf{v}^{\varepsilon_0,i}(z_2,\mathbf{y}) \equiv \mathbf{v}^{\varepsilon_0,i}(\boldsymbol{\zeta}_{\varepsilon_0}((0,z_2),\mathbf{y})$ is used (and similarly for $\boldsymbol{\tau}^i$) and where $\mathbf{v}^{\varepsilon_0,i}$ and $\boldsymbol{\tau}^{\varepsilon_0,i}$ are sought in $\boldsymbol{\mathcal{V}}$, i.e. they must contain only fast variations in y_2.

We work at ε_0 fixed and, to ease the notations, the ε_0 dependency of $\mathbf{u}^{\varepsilon_0,i}$, $\mathbf{v}^{\varepsilon_0,i}$, $\boldsymbol{\sigma}^{\varepsilon_0,i}$ and $\boldsymbol{\tau}^{\varepsilon_0,i}$ is dropped in the following. Nevertheless, one must keep in mind that the whole solution, even the leading term, depends on a particular choice of ε_0.

Deriving the equation driving the asymptotic coefficients is very similar to the periodic case. Nevertheless, the $\mathbf{x}$ divergence for tensors belonging to $\boldsymbol{\Gamma}_s^{\varepsilon}$ in $\mathbf{x}$ needs to be clarify. First, let us remind that, for the general case, the gradient of a vector $\mathbf{h}(\mathbf{x})$ is defined as

$$\boldsymbol{\nabla}_{\mathbf{x}}\mathbf{h} \equiv \frac{\partial\mathbf{h}}{\partial z^\alpha}\otimes\mathbf{g}^\alpha\,, \tag{105}$$

where $\mathbf{g}^\alpha$ is the contravariant curvilinear basis vectors. Thanks to the orthonormality of the curvilinear basis vectors in the vicinity of $\boldsymbol{\Gamma}_s^{\varepsilon_0}$, we have $\mathbf{g}^\alpha = \mathbf{g}_\alpha$. The gradient along a curvilinear vector basis,

can be written

$$\mathbf{g}_\alpha \cdot \boldsymbol{\nabla}_{\mathbf{x}} \mathbf{h} \equiv (\boldsymbol{\nabla}_{\mathbf{x}} \mathbf{h}) \cdot \mathbf{g}_\alpha \,, \tag{106}$$

$$= \frac{\partial \mathbf{h}}{\partial z^\beta} \left(\mathbf{g}^\beta \cdot \mathbf{g}_\alpha\right), \tag{107}$$

$$= \frac{\partial \mathbf{h}}{\partial z_\alpha} \,. \tag{108}$$

We can now define the $\mathbf{x}$ divergence for any tensor $\mathbf{d}(z_2)$ belonging to $\boldsymbol{\Gamma}_s^\varepsilon$ (i.e. doesn't depend on z_1),

$$\boldsymbol{\nabla}_{\mathbf{g}_2} \cdot \mathbf{d} \equiv (\mathbf{g}_2 \cdot \boldsymbol{\nabla}_{\mathbf{x}} \mathbf{d}) \cdot \mathbf{g}_2 = \frac{\partial \mathbf{d}}{\partial z_2} \cdot \mathbf{g}_2 = \boldsymbol{\nabla}_{\mathbf{x}} \cdot \mathbf{d} \,. \tag{109}$$

Similarly, for any vector $\mathbf{h}(z_2)$ belonging to $\boldsymbol{\Gamma}_s^\varepsilon$ in $\mathbf{x}$,

$$\boldsymbol{\epsilon}_{\mathbf{g}_2}(\mathbf{h}) \equiv \frac{1}{2}\left(\frac{\partial \mathbf{h}}{\partial z_2} \otimes \mathbf{g}_2 + \mathbf{g}_2 \otimes \frac{\partial \mathbf{h}}{\partial z_2}\right) = \boldsymbol{\epsilon}_{\mathbf{x}}(\mathbf{h}) \,. \tag{110}$$

Following the same classical procedure as for the periodic case, we easily obtain the asymptotic equations:

- equations in the volume $\boldsymbol{\Omega}_s^{\varepsilon_0}$, for $i \geq -2$:

$$\rho \partial_{tt} \mathbf{u}^i - \boldsymbol{\nabla}_{\mathbf{x}} \cdot \boldsymbol{\sigma}^i = \boldsymbol{f} \delta_{i0} \quad \text{in} \quad \boldsymbol{\Omega}_s^{\varepsilon_0} \,, \tag{111}$$

$$\boldsymbol{\sigma}^i = \mathbf{c} : \boldsymbol{\epsilon}_x\left(\mathbf{u}^i\right) \quad \text{in} \quad \boldsymbol{\Omega}_s^{\varepsilon_0} \tag{112}$$

$$\lim_{x_1 \to \infty} \boldsymbol{\sigma}^i \cdot \hat{\mathbf{x}}_1 = \mathbf{0} \,. \tag{113}$$

- equation in the boundary layer:

$$\rho \partial_{tt} \mathbf{v}^i - \boldsymbol{\nabla}_{\mathbf{g}_2} \cdot \boldsymbol{\tau}^i - \boldsymbol{\nabla}_{\mathbf{y}} \cdot \boldsymbol{\tau}^{i+1} = \boldsymbol{f} \delta_{i0} \quad \text{in} \quad \mathbb{R} \times \mathbb{Y}_{\mathbf{z}} \,,\ i \geq -2 \,, \tag{114}$$

$$\boldsymbol{\tau}^i = \mathbf{c} : \left(\boldsymbol{\epsilon}_{\mathbf{g}_2}\left(\mathbf{v}^i\right) + \boldsymbol{\epsilon}_{\mathbf{y}}\left(\mathbf{v}^{i+1}\right)\right) \quad \text{in} \quad \mathbb{R} \times \mathbb{Y}_{\mathbf{z}} \,,\ i \geq -1 \tag{115}$$

$$\boldsymbol{\tau}^i \cdot \mathbf{n} = 0 \text{ on } \mathbb{R} \times \boldsymbol{\Gamma}^{\varepsilon_0} \ i \geq 0. \tag{116}$$

The matching conditions need a special care and their development is given in appendix B. The two first orders are

- order 0:

$$\begin{aligned} &\lim_{y_1 \to \infty} \left(\mathbf{v}^0(z_2, y_1, y_2) - \mathbf{u}^0(\mathbf{x})\right) = 0 \,, \\ &\lim_{y_1 \to \infty} \left(\boldsymbol{\tau}^0(z_2, y_1, y_2) - \boldsymbol{\sigma}^0(\mathbf{x})\right) = 0 \,; \end{aligned} \tag{117}$$

- order 1:

$$\begin{aligned} &\lim_{y_1 \to \infty} \left(\mathbf{v}^1(z_2, y_1, y_2) - \mathbf{u}^1(\mathbf{x}) - y_1 \left(\mathbf{g}_1 \cdot \boldsymbol{\nabla}_{\mathbf{x}}\right) \mathbf{u}^0(\mathbf{x})\right) = 0 \,, \\ &\lim_{y_1 \to \infty} \left(\boldsymbol{\tau}^1(z_2, y_1, y_2) - \boldsymbol{\sigma}^1(\mathbf{x}) - y_1 \left(\mathbf{g}_1 \cdot \boldsymbol{\nabla}_{\mathbf{x}}\right) \boldsymbol{\sigma}^0(\mathbf{x})\right) = 0 \,; \end{aligned} \tag{118}$$

with $\mathbf{x} = \boldsymbol{\zeta}_{\varepsilon_0}((0, z_2))$ in (117) and (118).

3.2 Iterative resolution of the asymptotic equations

We now solve the asymptotic equations for the order 0 and for the first order corrector.

3.2.1 Order 0

At this stage, the periodic-case and non-periodic case equations are the same and therefore, the resolution can be followed identically. The only point that needs some attention is when an integration by part is used over the cell domain $\mathbb{Y}_{\mathbf{z}}$. Indeed, for a general transformation $\boldsymbol{\zeta}_{\varepsilon_0}$ the outward normal $\mathbf{n}_{\mathbf{y}}$ to $\partial\mathbb{Y}_{\mathbf{z}}$ is not the same as $\mathbf{n}$ the outward normal to $\boldsymbol{\Omega}_{\mathbf{x}}$. Nevertheless, as mentioned in Sec. 3.1, the transformation $\boldsymbol{\zeta}_{\varepsilon_0}$ is built such that the curvilinear coordinate system is orthogonal around the effective free surface. As the free surface is in the neighborhood of the effective free surface, $\mathbf{n}_{\mathbf{y}}$ and $\mathbf{n}$ are collinear and the boundary condition $\boldsymbol{\tau}^i \cdot \mathbf{n}_{\mathbf{y}} = 0$ on $\boldsymbol{\Gamma}^{\varepsilon}(\mathbf{x}, \mathbf{y})$ is valid. Knowing this, we easily find

$$\mathbf{v}^0(z_2, \mathbf{y}) = \mathbf{v}^0(z_2)\,, \tag{119}$$

$$\boldsymbol{\tau}^{-1} = 0\,. \tag{120}$$

The order 0 matching condition for the displacement yields:

$$\mathbf{u}^0(0, z_2) = \mathbf{v}^0(z_2)\,. \tag{121}$$

For the order 0 boundary condition, by the same token as for the periodic case and knowing that $\hat{\mathbf{y}}_1 = \mathbf{g}_1$ for $\mathbf{x}$ on the effective interface, we find ($\mathbf{g}_1$ is the inward normal to $\boldsymbol{\Gamma}_s^{\varepsilon_0}$),

$$\boldsymbol{\sigma}^0(\mathbf{x}) \cdot \mathbf{g}_1 = 0 \quad \text{for } \mathbf{x} \in \boldsymbol{\Gamma}_s^{\varepsilon_0}. \tag{122}$$

3.2.2 Order 1

The order 1 development is very similar to the periodic case, but for the details very little of the development can be avoided. Eq. (111) for $i = -1$ and Eq. (112) for $i = 0$ yield:

$$\boldsymbol{\nabla}_{\mathbf{y}} \cdot \boldsymbol{\tau}^0 = 0\,, \tag{123}$$

$$\boldsymbol{\tau}^0 = \mathbf{c} : \left(\boldsymbol{\epsilon}_{\mathbf{g}_2}(\mathbf{v}^0) + \boldsymbol{\epsilon}_{\mathbf{y}}(\mathbf{v}^1)\right)\,. \tag{124}$$

We seek for solutions to the last equations as

$$\mathbf{v}^1(z_2, \mathbf{y}) = y_1(\mathbf{g}_1 \cdot \boldsymbol{\nabla}_{\mathbf{x}})\mathbf{u}^0 + \hat{\mathbf{v}}(z_2, \mathbf{y}) = y_1 \frac{\partial \mathbf{u}^0}{\partial z_1}(0, z_2) + \hat{\mathbf{v}}(z_2, \mathbf{y})\,, \tag{125}$$

$$\boldsymbol{\tau}^0(z_2, \mathbf{y}) = \boldsymbol{\sigma}^0(0, z_2) + \hat{\boldsymbol{\tau}}(z_2, \mathbf{y})\,, \tag{126}$$

where $\hat{\mathbf{v}}$ and $\hat{\boldsymbol{\tau}}$ belongs to $\boldsymbol{\mathcal{V}}$. Using the fact that $\boldsymbol{\sigma}^0$ does not depend on $\mathbf{y}$, (123) easily gives us

$$\boldsymbol{\nabla}_{\mathbf{y}} \cdot \hat{\boldsymbol{\tau}} = 0\,. \tag{127}$$

Using (121), (110) and the fact that $\boldsymbol{\nabla}_{\mathbf{y}} y_1 = \hat{\mathbf{y}}_1 = \mathbf{g}_1$, we have, on $\boldsymbol{\Gamma}_s$

$$\boldsymbol{\epsilon}_{\mathbf{y}}\left(y_1(\mathbf{g}_1 \cdot \boldsymbol{\nabla}_{\mathbf{x}})\mathbf{u}^0\right) + \boldsymbol{\epsilon}_{\mathbf{g}_2}(\mathbf{v}^0) = \boldsymbol{\epsilon}_{\mathbf{x}}(\mathbf{u}^0)\,, \tag{128}$$

then, (125) and the last equation yield

$$\boldsymbol{\tau}^0 = \mathbf{c} : \left(\boldsymbol{\epsilon}_{\mathbf{x}}(\mathbf{u}^0) + \boldsymbol{\epsilon}_{\mathbf{y}}(\hat{\mathbf{v}})\right)\,, \tag{129}$$

$$= \boldsymbol{\sigma}^0 + \mathbf{c} : \boldsymbol{\epsilon}_{\mathbf{y}}(\hat{\mathbf{v}})\,. \tag{130}$$

Using the boundary condition (116), the order 1 asymptotic problem reduces to the following problem:

$$\hat{\boldsymbol{\tau}} = \mathbf{c} : \boldsymbol{\epsilon}_{\mathbf{y}}(\hat{\mathbf{v}}) \quad \text{in} \quad \mathbb{R} \times \mathbb{Y}_{\mathbf{z}}\,, \tag{131}$$

$$\boldsymbol{\nabla}_{\mathbf{y}} \cdot \hat{\boldsymbol{\tau}} = \mathbf{0} \quad \text{in} \quad \mathbb{R} \times \mathbb{Y}_{\mathbf{z}}\,, \tag{132}$$

$$\hat{\boldsymbol{\tau}} \cdot \mathbf{n} = -\boldsymbol{\sigma}^0(0, z_2) \cdot \mathbf{n} \quad \text{on} \quad \mathbb{R} \times \boldsymbol{\Gamma}^{\varepsilon_0}\,, \tag{133}$$

$$\lim_{y_1 \to \infty} \hat{\boldsymbol{\tau}} \cdot \hat{\mathbf{y}}_1 = \mathbf{0}\,, \tag{134}$$

$$\hat{\mathbf{v}}(z_2, \mathbf{y}) \quad \text{and} \quad \hat{\boldsymbol{\tau}}(z_2, \mathbf{y}) \quad \text{are in } \boldsymbol{\mathcal{V}}\,. \tag{135}$$

Based on the linearity of the last problem and noting that the only non zero component of $\boldsymbol{\sigma}^0$ is $\sigma^0_{\mathbf{g}_2\mathbf{g}_2}(0, z_2) \equiv \mathbf{g}_2 \cdot \boldsymbol{\sigma}^0 \cdot \mathbf{g}_2$, we seek for solutions under the following form:

$$\hat{\mathbf{v}}(z_2, \mathbf{y}) = \sigma^0_{\mathbf{g}_2\mathbf{g}_2}(0, z_2)\mathbf{V}(z_2, \mathbf{y}) + \langle \hat{\mathbf{v}} \rangle (z_2) \tag{136}$$

$$\hat{\boldsymbol{\tau}}(z_2, \mathbf{y}) = \sigma^0_{\mathbf{g}_2\mathbf{g}_2}(0, z_2)\mathbf{T}(z_2, \mathbf{y})\,, \tag{137}$$

where $\mathbf{V}$ and $\mathbf{T}$ are in $\boldsymbol{\mathcal{V}}$. From equations (131–135), we show that $\mathbf{V}$ and $\mathbf{T}$ are solutions of the following cell problems:

$$\begin{cases} \mathbf{T} = \mathbf{c} : \boldsymbol{\epsilon}_{\mathbf{y}}(\mathbf{V}) \quad \text{in} \quad \mathbb{R} \times \mathbb{Y}_{\mathbf{z}}\,, \\ \boldsymbol{\nabla}_{\mathbf{y}} \cdot \mathbf{T} = \mathbf{0} \quad \text{in} \quad \mathbb{R} \times \mathbb{Y}_{\mathbf{z}}\,, \\ \mathbf{T} \cdot \mathbf{n} = -(\mathbf{n} \cdot \hat{\mathbf{y}}_2)\,\hat{\mathbf{y}}_2 \quad \text{on} \quad \mathbb{R} \times \boldsymbol{\Gamma}^{\varepsilon_0}\,, \\ \lim\limits_{y_1 \to \infty} \mathbf{T} \cdot \hat{\mathbf{y}}_1 = \mathbf{0}\,. \\ \mathbf{T} \quad \text{and} \quad \mathbf{V} \quad \text{in } \boldsymbol{\mathcal{V}}. \end{cases} \tag{138}$$

The last problem can be solved based on the same finite elements solver as for the periodic case. It is actually the same problem as for the periodic case but in a deformed geometry resulting of the $\boldsymbol{\zeta}_{\varepsilon_0}$ transformation. We are now able to compute $\hat{\boldsymbol{\tau}}$ and incompletely $\hat{\mathbf{v}}$ ($\langle \hat{\mathbf{v}} \rangle$ is not determined).

We now need to compute the order 1 boundary for the volume. This development is very similar to

the periodic case, nevertheless, we need to go through it again to account for the deformed geometry. The external source $\boldsymbol{f}$ is once again assumed to be in the volume domain, and is reintroduced later if this is not the case. Integrating the stress matching condition for $i = 1$ over Y_w, we find

$$|Y_w|\,\boldsymbol{\sigma}^1(0,z_2) = \lim_{y_1\to\infty}\left(\int_{Y_w}\boldsymbol{\tau}^1(z_2,\mathbf{y})\,dy_2 - y_1|Y_w|(\mathbf{g}_1\cdot\boldsymbol{\nabla}_{\mathbf{x}})\boldsymbol{\sigma}^0(0,z_2)\right). \tag{139}$$

Eq. (114) for $i = 0$ gives

$$\boldsymbol{\nabla}_{\mathbf{y}}\cdot\boldsymbol{\tau}^1 = \rho\ddot{\mathbf{v}}^0 - \boldsymbol{\nabla}_{\mathbf{g}_2}\cdot\boldsymbol{\tau}^0\,, \tag{140}$$

and therefore,

$$\boldsymbol{\nabla}_{\mathbf{y}}\cdot\boldsymbol{\tau}^1 + \boldsymbol{\nabla}_{\mathbf{g}_2}\cdot\boldsymbol{\sigma}^0(0,z_2) + \boldsymbol{\nabla}_{\mathbf{g}_2}\cdot\hat{\boldsymbol{\tau}} = \rho\ddot{\mathbf{v}}^0\,. \tag{141}$$

Using the definition (93) of $\mathbb{Y}_{\mathbf{z}}$, we have $\partial_{z_2}\mathbb{Y}_{\mathbf{z}} = O(\varepsilon)$ and therefore,

$$\boldsymbol{\nabla}_{\mathbf{g}_2}\cdot\int_{\mathbb{Y}_{\mathbf{z}}}\hat{\boldsymbol{\tau}}d\mathbf{y} = \int_{\mathbb{Y}_{\mathbf{z}}}\boldsymbol{\nabla}_{\mathbf{g}_2}\cdot\hat{\boldsymbol{\tau}}d\mathbf{y} + O(\varepsilon)\,. \tag{142}$$

Using (121), integrating (141) over $\mathbb{Y}_{\mathbf{z}}(y_1)$ and passing to the limit and using the last equation, we obtain, to the first order,

$$\boldsymbol{\nabla}_{\mathbf{g}_2}\cdot\int_{\mathbb{Y}_{\mathbf{z}}}\hat{\boldsymbol{\tau}}d\mathbf{y} = \lim_{y_1\to\infty}\left(-\int_{\mathbb{Y}_{\mathbf{z}}(y_1)}\boldsymbol{\nabla}_{\mathbf{y}}\cdot\boldsymbol{\tau}^1 d\mathbf{y}' + |\mathbb{Y}_{\mathbf{z}}(y_1)|\left(-\boldsymbol{\nabla}_{\mathbf{g}_2}\cdot\boldsymbol{\sigma}^0 + \rho\ddot{\mathbf{u}}^0\right)\right). \tag{143}$$

Using an integration by parts, the free boundary condition along $\boldsymbol{\Gamma}$ and the periodicity in y_2, we find

$$\int_{\mathbb{Y}_{\mathbf{z}}(y_1)}\boldsymbol{\nabla}_{\mathbf{y}}\cdot\boldsymbol{\tau}^1(z_2,\mathbf{y}')\,d\mathbf{y}' = \int_{Y_w}\boldsymbol{\tau}^1(z_2,y_1,y_2)\cdot\mathbf{g}_1\,dy_2\,. \tag{144}$$

Using (144) and (139) in (143), we have

$$\boldsymbol{\nabla}_{\mathbf{g}_2}\cdot\int_{\mathbb{Y}_{\mathbf{z}}}\hat{\boldsymbol{\tau}}d\mathbf{y} = -|Y_w|\boldsymbol{\sigma}^1\cdot\mathbf{g}_1 + \lim_{y_1\to\infty}\left(-y_1|Y_w|(\mathbf{g}_1\cdot\boldsymbol{\nabla}_{\mathbf{x}})\boldsymbol{\sigma}^0\cdot\mathbf{g}_1 + |\mathbb{Y}_{\mathbf{z}}(y_1)|\left(-\boldsymbol{\nabla}_{\mathbf{g}_2}\cdot\boldsymbol{\sigma}^0 + \rho\ddot{\mathbf{u}}^0\right)\right), \tag{145}$$

where $|\mathbb{Y}_{\mathbf{z}}(y_1)| = \int_{\mathbb{Y}_{\mathbf{z}}(y_1)} d\mathbf{y}'$. Using (111) for $i = 0$ and $(\mathbf{g}_1\cdot\boldsymbol{\nabla}_{\mathbf{x}})\boldsymbol{\sigma}^0\cdot\mathbf{g}_1 = \boldsymbol{\nabla}_{\mathbf{g}_1}\cdot\boldsymbol{\sigma}^0$ in the last equation, we get

$$\boldsymbol{\nabla}_{\mathbf{g}_2}\cdot\int_{\mathbb{Y}_{\mathbf{z}}}\hat{\boldsymbol{\tau}}d\mathbf{y} = -|Y_w|\,\boldsymbol{\sigma}^1\cdot\mathbf{g}_1 + \lim_{y_1\to\infty}(|\mathbb{Y}_{\mathbf{z}}(y_1)| - y_1|Y_w|)\left(-\boldsymbol{\nabla}_{\mathbf{g}_2}\cdot\boldsymbol{\sigma}^0 + \rho\ddot{\mathbf{u}}^0\right), \tag{146}$$

which finally leads to the order 1 volume boundary condition on $\boldsymbol{\Gamma}_s^{\varepsilon_0}$,

$$\varepsilon\boldsymbol{\sigma}^1(0,z_2)\cdot\mathbf{g}_1 = -\frac{\partial}{\partial z_2}(\sigma^0_{\mathbf{g}_2\mathbf{g}_2}\,\mathbf{b}(z_2)) + h(z_2)\left(-\boldsymbol{\nabla}_{g_2}\cdot\boldsymbol{\sigma}^0 + \rho\ddot{\mathbf{u}}^0\right), \tag{147}$$

where

$$\mathbf{b}(z_2) = \frac{\varepsilon}{|Y_w|} \int_{\mathbb{Y}_\mathbf{z}} \mathbf{T} \cdot \hat{\mathbf{y}}_2 \, d\mathbf{y} \,, \tag{148}$$

$$h(z_2) = \varepsilon \lim_{y_1 \to \infty} \frac{|\mathbb{Y}_\mathbf{z}(y_1)| - y_1 |Y_w|}{|Y_w|} \,. \tag{149}$$

Based on the same demonstration as for the periodic case, we show that $\mathbf{b} \cdot \hat{\mathbf{y}}_1 = 0$. Using again the fact that only $\sigma^0_{\mathbf{g}_2\mathbf{g}_2}$ is non zero on $\mathbf{\Gamma}_s$, we can rewrite the order 1 boundary condition on $\mathbf{\Gamma}_s$ as:

$$\varepsilon \boldsymbol{\sigma}^1(0, z_2) \cdot \mathbf{g}_1 = \left\{ -\frac{\partial}{\partial z_2} \left((\mathbf{b} \cdot \hat{\mathbf{y}}_2 + h) \sigma^0_{\mathbf{g}_2\mathbf{g}_2} \, \mathbf{g}_2 \right) + \frac{\partial h}{\partial z_2} \boldsymbol{\sigma}^0 \cdot \mathbf{g}_2 + h \rho \ddot{\mathbf{u}}^0 \right\}_{\mathbf{z}=(0,z_2)} \,. \tag{150}$$

Using the fact that $\partial_{z_2} h = O(\varepsilon)$, the last equation can also be written, to the first order:

$$\varepsilon \boldsymbol{\sigma}^1(0, z_2) \cdot \mathbf{g}_1 = \left\{ - \left(\mathbf{g}_2 \cdot \boldsymbol{\nabla}_\mathbf{x} \right) \left(\left((\mathbf{b}(z_2) \cdot \hat{\mathbf{y}}_2 + h) \, \mathbf{g}_2 \cdot \boldsymbol{\sigma}^0 \cdot \mathbf{g}_2 \right) \mathbf{g}_2 \right) + h(z_2) \rho \ddot{\mathbf{u}}^0 \right\}_{\mathbf{z}=(0,z_2)} \,. \tag{151}$$

3.3 Construction of $\boldsymbol{\zeta}_{\varepsilon_0}$

Assuming $\mathbf{\Gamma}_s^{\varepsilon_0}$ is known, following Fletcher (1991) and Komatitsch *et al.* (1996), we use a simple algebraic method based on third degree Hermite polynomials allowing to obtain an orthonormal curvilinear basis vector in the neighborhood of $\mathbf{\Gamma}_s^{\varepsilon_0}$. This allows to build a parametric transformation $\boldsymbol{\zeta}_{\varepsilon_0}$. The inverse transformation $\boldsymbol{\zeta}_{\varepsilon_0}^{-1}$ is not known analytically, but can be built numerically.

3.4 Finding $\mathbf{\Gamma}_s^{\varepsilon_0}$ and consequences

Now that we have shown how to write and solve the matched asymptotic problem for the non-periodic case, the main point of this paper is to find a smooth effective topography $\mathbf{\Gamma}_s^{\varepsilon_0}$ that will define the transformation $\boldsymbol{\zeta}_{\varepsilon_0}$ such that $\mathbf{T}$ and $\mathbf{V}$ indeed belong to $\boldsymbol{\mathcal{V}}$. We will not try to show that such a smooth effective topography $\mathbf{\Gamma}_s^{\varepsilon_0}$ exits in general or that there is some kind of uniqueness up to a constant of the solution, if any. We just show that it is possible to find a solution in some cases and that those cases include all the examples we have tried. A solution to find $\mathbf{\Gamma}_s^{\varepsilon_0}$ could be to set up optimization algorithm, but that would be probably difficult. Instead, we propose an intuitive iterative approach for which we need to define, for any tensor $\mathbf{t}(\mathbf{y})$ in $\mathbb{Y}_\mathbf{z}$ and extended to $\mathbb{R}^2$ with zeros,

$$\bar{\mathcal{F}}\left(\mathbf{t}\right)(y_2) \equiv \int_{\mathbb{Y}_\mathbf{z}} w_m(y_2 - y_2') \mathbf{t}(y_1', y_2') \, d\mathbf{y}' \,. \tag{152}$$

$$= \int_{\mathbb{R}} \mathcal{F}\left(\mathbf{t}\right)(y_1, y_2) \, dy_1 \,. \tag{153}$$

$\bar{\mathcal{F}}\left(\mathbf{t}\right)(y_2)$ is the sum along y_1 of all $\mathbf{t}$ lowpass filtered cross sections along y_2. Moreover, we define

$$\bar{\mathcal{F}}_a\left(\mathbf{t}\right)(y_2) = \int_{\mathbb{Y}_\mathbf{z}, y_1 \geq 0} w_m(y_2 - y_2') \mathbf{t}(y_1', y_2') \, d\mathbf{y}' \,, \tag{154}$$

and

$$\bar{\mathcal{F}}_b\left(\mathbf{t}\right)\left(y_2\right)=\int_{\mathbb{Y}_{\mathbf{z}},y_1<0} w_m(y_2-y_2')\mathbf{t}(y_1',y_2')\,d\mathbf{y}'\,, \tag{155}$$

such $\bar{\mathcal{F}}\left(\mathbf{t}\right)=\bar{\mathcal{F}}_a\left(\mathbf{t}\right)+\bar{\mathcal{F}}_b\left(\mathbf{t}\right)$.

We propose to take advantage of the following property (see appendix C):

$$\bar{\mathcal{F}}\left(T_{22}\right)=\bar{\mathcal{F}}_a\left(T_{22}\right)+\bar{\mathcal{F}}_b\left(T_{22}\right)=\mathcal{F}\left(\Gamma^{\varepsilon_0}\right)\,. \tag{156}$$

Note that $\mathcal{F}\left(\Gamma^{\varepsilon_0}\right)$ is simply the lowpass filtered topography. The last equation therefore means that the lowpass filtered topography is equal to $\bar{\mathcal{F}}\left(T_{22}\right)$. The idea is the following: if $\mathbf{T}$ belongs to $\boldsymbol{\mathcal{V}}$, then $\mathcal{F}\left(T_{22}\right)\left(y_1,y_2\right)=cst$ for $y_1\geq 0$, where cst is a constant value in y_2. Assuming, for the sake of simplicity, that $\int cst\,dy_1=0$, $\mathbf{T}$ belongs to $\boldsymbol{\mathcal{V}}$ therefore implies that $\bar{\mathcal{F}}_b\left(T_{22}\right)=0$. Even if $\bar{\mathcal{F}}_b\left(T_{22}\right)=0$ is not a warranty that $\mathbf{T}$ belongs to $\boldsymbol{\mathcal{V}}$, we at least need to find an effective topography such that $\bar{\mathcal{F}}_b\left(T_{22}\right)=0$. For a wrong effective topography, $\bar{\mathcal{F}}_b\left(T_{22}\right)$ is not zero and, based on (156), we make the assumption, that we just need to remove $\bar{\mathcal{F}}_b\left(T_{22}\right)$ from $\mathcal{F}\left(\Gamma^{\varepsilon_0}\right)$ and to iterate this process to obtain the wanted results. With such an idea, we propose the following scheme:

(i) iteration $iter=0$; We assume a flat effective free surface at start. Therefore, we build a flat $\Gamma_s^{\varepsilon_0,iter=0}$ interface and build the associate transformation $\boldsymbol{\zeta}_{\varepsilon_0}^{iter=0}$ as well as its inverse $\left[\boldsymbol{\zeta}_{\varepsilon_0}^{iter=0}\right]^{-1}$ (see Sec. 3.3).

(ii) build $\mathbb{Y}_{\mathbf{z}}^{iter}=[\boldsymbol{\zeta}_{\varepsilon_0}^{iter}]^{-1}(\boldsymbol{\Omega}^0)\cap\sqcap_{\mathbf{z}}$ finite element mesh, where $\sqcap_{\mathbf{z}}=\left\{\mathbf{y}\in\mathbb{R}^2;\,y_2\in[\varepsilon z_2-\beta\lambda_m,\,\varepsilon z_2+\beta\lambda_m]\right\}$

(iii) solve the cell problem (138) for $\mathbf{T}^{iter}$;

(iv) compute $\bar{\mathcal{F}}_b\left(T_{22}^{iter}\right)$ and deduce $\Gamma_s^{\varepsilon_0,iter+1}(\mathbf{x})=\bar{\mathcal{F}}_b\left(T_{22}\right)\left(\boldsymbol{\zeta}_{\varepsilon_0}^{iter}(\varepsilon\mathbf{y})\right)$

(v) if $\bar{\mathcal{F}}_b\left(T_{22}^{iter}\right)$ is small enough, the process is over; if not, build $\boldsymbol{\zeta}_{\varepsilon_0}^{iter+1}$ from $\Gamma_s^{\varepsilon_0,iter+1}(\mathbf{x})$ and go to (ii).

As we will show for an example in Sec. 3.7, and for all the examples we have tried, following this scheme, we find $\bar{\mathcal{F}}_b\left(T_{22}\right)=0$, but also $\mathbf{T}$ in $\boldsymbol{\mathcal{V}}$.

Once an appropriate effective topography is found, the problem is not solved yet. Indeed, depending on the chosen width of $\mathbb{Y}_{\mathbf{z}}$ and on the topography, the coefficients $\mathbf{b}(z_2)$ and $h(z_2)$ are not really smooth and can contain order 1 discontinuities. For a direct solver this can be a problem and smoother coefficients would be appropriate. This problem is another matched asymptotic problem. Its resolution is simple and leads to a cell problem similar to (138). The difference is that we have a smooth topography with an independent fast boundary condition (and not a fast topography and boundary condition that depends on this topography as it is the case for (138)). The homogenization problem is therefore linear with respect to the coefficient $\mathbf{b}$ and h which means that homogenization problem is trivial.

In such a case, the scale separation can be done with any king of linear filtering on $\mathbf{b}$ and h to find effective coefficients $\mathbf{b}^*$ and h^*. The fact that this second homogenization has to be done to obtain $\mathbf{b}^*$ and h^* is not very satisfactory and one could hope to obtain these effective coefficients form the effective topography in a single step. Unfortunately, we haven't any found alternative algorithm so far.

In practice, solving the cell problem (138) on a large number of small domains $\mathbb{Y}_{\mathbf{z}}$ is technically not straightforward because it imposes to design a large number of small meshes. Meshing tool efficient manipulations requires some skills that the authors don't have and we prefer an alternate strategy that is not fully equivalent and probably numerically less efficient but is easier to implement and that gives good results. Instead of a large number of small domains, we use the above iterative scheme on the whole domain at once, or on a few smaller domains (for parallel computing reasons for example). Once the effective topography is found, we compute the effective coefficients as

$$h^\star = \mathcal{F}_{m'}\left(h\right) , \tag{157}$$

$$\mathbf{b}^\star = \mathcal{F}_{m'}\left(\mathbf{b}\right) , \tag{158}$$

where, for any $\mathbf{t}$

$$\mathcal{F}_{m'}\left(\mathbf{t}\right)\left(z_2\right) = \frac{1}{\varepsilon_0}\int_{\mathbb{R}} \mathbf{t}(z_2')w_{m'}\left(\frac{z_2 - z_2'}{\varepsilon_0}\right) dz_2' , \tag{159}$$

and $w_{m'}$ is a lowpass filter with a $k_{m'}$ wave number cutoff that can be different from the cutoff k_m used in Sec. 3.1. Property (156) is still valid, which means that $\mathbf{h}^\star + b_2^\star = 0$. Therefore, finally, the order 1 boundary condition on $\mathbf{\Gamma}_s^{\varepsilon_0}$ reduces to

$$\varepsilon\boldsymbol{\sigma}^1(0, z_2)\cdot\mathbf{g}_1 = h^\star(z_2)\rho\ddot{\mathbf{u}}^0|_{\mathbf{z}=(0,z_2)} . \tag{160}$$

$k_{m'}$ could be used to define another small parameter ε_1, but we do not investigate this possibility and set $k_{m'} = k_m$ and, in this paper, we therefore have $\varepsilon_1 = \varepsilon_0$. To conclude, let us say that, if the calculus for the non-periodic case is more difficult than for the periodic case, the result for the boundary condition is the same. The new aspect is that the effective topography needs to be evaluate which is not as simple as for the periodic case.

3.5 Practical resolution of the effective equations

The different orders of the asymptotic expansion are combined together as it is done for the periodic case in Sec. 2.4. The order one correction for the receiver can be done as for the periodic case, and the external source, if within the boundary layer, is corrected using an energy principle as proposed in Sec. 2.4.1.

The only value of ε that has a physical meaning is $\varepsilon = \varepsilon_0$ as it is the only case for which the

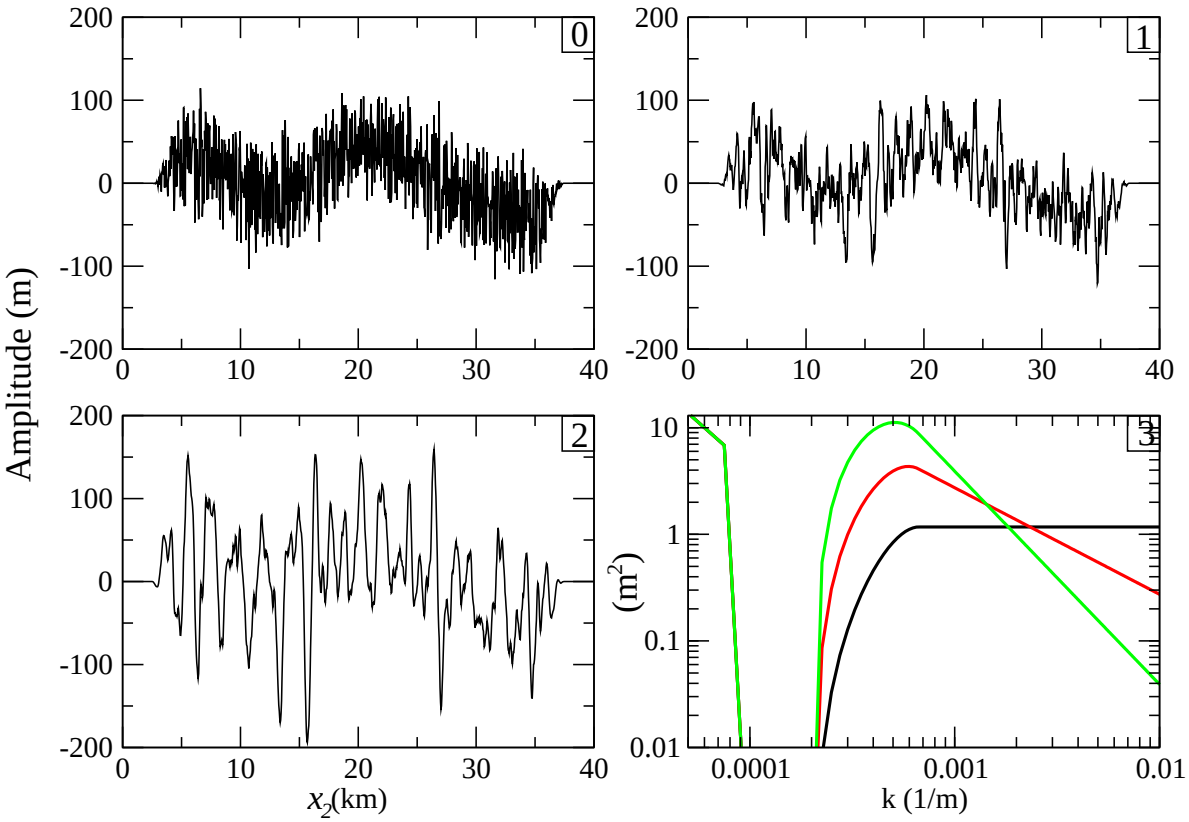

Figure 7. Graphs 0, 1 and 2: the three tested topographies $\mathbf{\Gamma}^0$. In graph 3 is plotted the module of the spectrum of each topography (black: topography 0; red: topography 1; green: topography 2)

solution to the ε-indexed set of solutions $\mathbf{u}^{\varepsilon_0,\varepsilon}$ is equal to the solution of the original problem $\mathbf{u}^{ref}$. We therefore in practice always have $\varepsilon_0 = \varepsilon$. This has a practical consequence on the type of topography for which we can have a warranted convergence of the asymptotic solution toward $\mathbf{u}^{ref}$ with ε_0. Indeed, depending of the spectrum of the topography, the amplitude of $\mathbf{\Gamma}^{\varepsilon_0}$ decreases or not with ε_0. If the topography spectrum is such that the amplitude of $\mathbf{\Gamma}^{\varepsilon_0}$ does not decrease with ε_0, we do not expect any convergence. This is a notable difference with the non-periodic homogenization in the volume (Capdeville *et al.*, 2010b) for which the convergence with ε_0 is independent on the property of the elastic media as long as a minimum wavelength can be defined.

We finally replace the original problem by solving the wave equation in the domain $\mathbf{\Omega}_s^{\varepsilon_0}$ with the dynamic boundary condition (160), which is simple to implement in a spectral element program. The effective topography $\mathbf{\Gamma}_s^{\varepsilon_0}$ nevertheless needs to be meshed, which is not as simple as for the periodic case, but a much simpler problem than meshing the original topography $\mathbf{\Gamma}_0$. The effective solutions depend on ε_0 and we expect the accuracy to increase when ε_0 decreases.

3.6 Validation tests

In this section, we test the non-periodic algorithm on three topographies shown on Fig. 7, graph 0, 1 and 2. Each of these three topographies have a low frequency component, and a high frequency component with the following type of spectrum:

- topography 0: flat high frequency spectrum;
- topography 1: k^{-1} high frequency spectrum;
- topography 2: k^{-2} high frequency spectrum.

The spectrum of each topography is plotted on Fig. 7, graph 3. It can be noted that the spectrum of topography 0 is flat for high wavenumber, which implies that there is little chance that the amplitude of $\mathbf{\Gamma}^{\varepsilon_0}$ decreases with ε_0 and therefore, as mentioned in Sec. 3.5, we expect, in that case, some difficulties for the convergence. Even if the earth large scale topography spectrum is more in k^{-2}, none of the tested topographies is supposed to be realistic, but they provide good tests for our method.

Before going further, let us define the average interface:

$$\Gamma_a^{\varepsilon_0} = \frac{1}{\varepsilon_0} \int_{\mathbb{R}} w_m \left(\frac{x_2 - x_2'}{\varepsilon_0} \right) \Gamma^{\varepsilon_0}(x_2')\, dx_2' \,. \tag{161}$$

Note that, if the average interface $\Gamma_a^{\varepsilon_0}$ is in general different from the effective interface $\Gamma_s^{\varepsilon_0}$, wave equation solutions computed using both topographies (with free boundary condition) are both order 0 solution. A ε_0 convergence can therefore be expected for both smooth interfaces if the original topography spectrum allows it.

3.7 Iterative algorithm to find the effective topography example

Before addressing the accuracy and convergence of the effective solution, we illustrate the algorithm proposed in Sec. 3.4. We choose the topography 0 (Fig. 7. graph 0) and run our algorithm for $\lambda_0 =$1 km. On Fig. 8, left graph, is shown $\bar{\mathcal{F}}_b\left(T_{22}^{iter}\right)$ for three iterations and, as expected its amplitude decreases toward zero with the number of iterations. At the end of the process, we indeed have found a smooth effective topography for which $\bar{\mathcal{F}}_b\left(T_{22}^{iter}\right) \simeq 0$. For each iteration, the new topography $\mathbf{\Gamma}^{\varepsilon_0}$ needs to be meshed. For that purpose, we use the tool *gmsh* (Geuzaine & Remacle, 2009) (see Fig. 9). On Fig. 8, right graph, are plotted the corresponding $\mathbf{\Gamma}_s^{\varepsilon_0}$ for the last iteration and, for comparison, the average interface $\mathbf{\Gamma}_a^{\varepsilon_0}$. It can be clearly seen that the effective interface is below the average interface and looks like a kind of lower envelope on the original topography. On Fig. 10, right plot, is shown a cut along the y_2 axis for $y_1 = 100m$ of $T_{22}^{iter}(\mathbf{y})$ for the first and the last iterations and on the right plot the corresponding spectrum. If the $T_{22}^{iter=1}$ doesn't belong to $\boldsymbol{\mathcal{V}}$ (a significant amplitude signal can be seen on its Fourier spectrum for $k < 0.001m^{-1}$), $T_{22}^{iter=5}$ is clearly in $\boldsymbol{\mathcal{V}}$ (The same observation

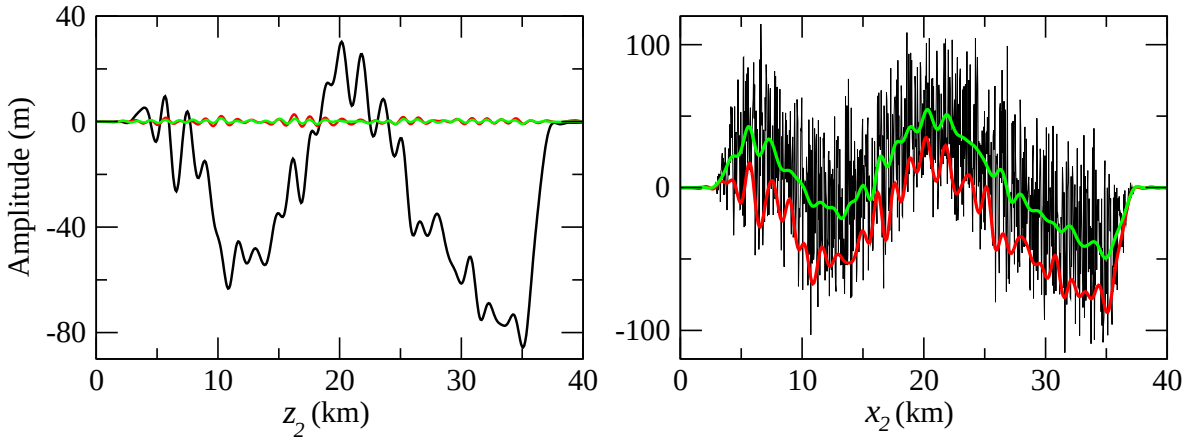

Figure 8. Left plot: $\bar{\mathcal{F}}_b\left(T_{22}^{iter}\right)$ for $iter = 1$ (black line), $iter = 3$ (red line) and $iter = 5$ (green line). Right plot: original topography $\mathbf{\Gamma}^0$ (black line), the effective topography $\mathbf{\Gamma}_s^{\varepsilon_0}$ for λ_0 =1 km after 5 iterations (red line) and, for comparison, the lowpass filtered topography for the same λ_0, $\mathbf{\Gamma}_a^{\varepsilon_0}$ (green line).

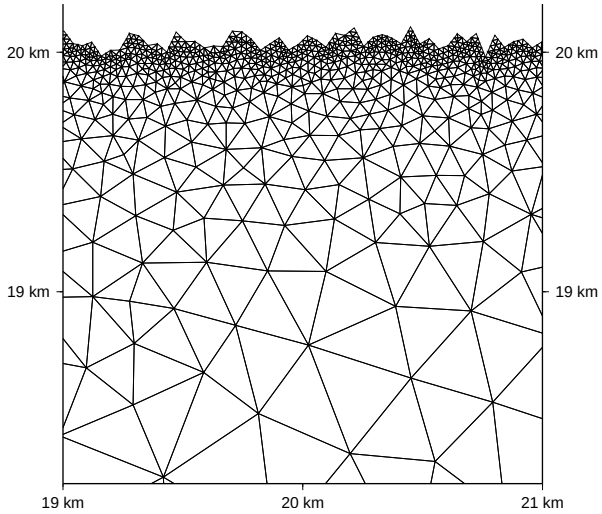

Figure 9. Finite element mesh sample used to solve the cell problem (138), for the first iteration of the algorithm described in Sec. 3.4, used to find the effective topography

could be made for T_{12}, if plotted). This shows the proposed algorithm can find an effective topography for which $\bar{\mathcal{F}}_b\left(\mathbf{T}\right) = 0$ and, moreover, it can find an effective topography for which $\mathbf{T}$ is in $\boldsymbol{\mathcal{V}}$. The convergence of this example and the fact that $\mathbf{T}$ numerically belongs to $\boldsymbol{\mathcal{V}}$ is representative of all the other tested topographies.

3.8 Accuracy and convergence of the effective solution

In this section, we use reference solutions computed with SEM, meshing the three original topographies, once again using *gmsh*, for an explosion located 200 m below the free surface. We then compute the average topographies $\mathbf{\Gamma}_a^{\varepsilon_0}$ and effective topographies $\mathbf{\Gamma}_s^{\varepsilon_0}$ for five values of ε_0. Samples of each of

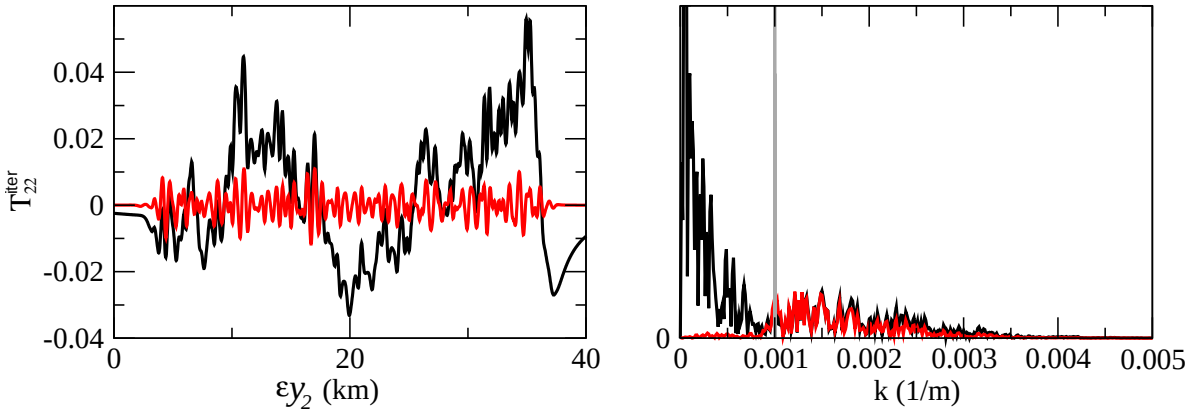

Figure 10. Left plot: $T_{22}(y_1, y_2)$ as a function of y_2 for a fixed y_1, 100 m below the effective topography for iterations 1 (black line) and 5 (red line). Right plot: corresponding module of the Fourier transform of $T_{22}(y_1, y_2)$ along y_2 for iterations 1 (black line) and 5 (red line). The grey line corresponds to $k_0 = 0.001$

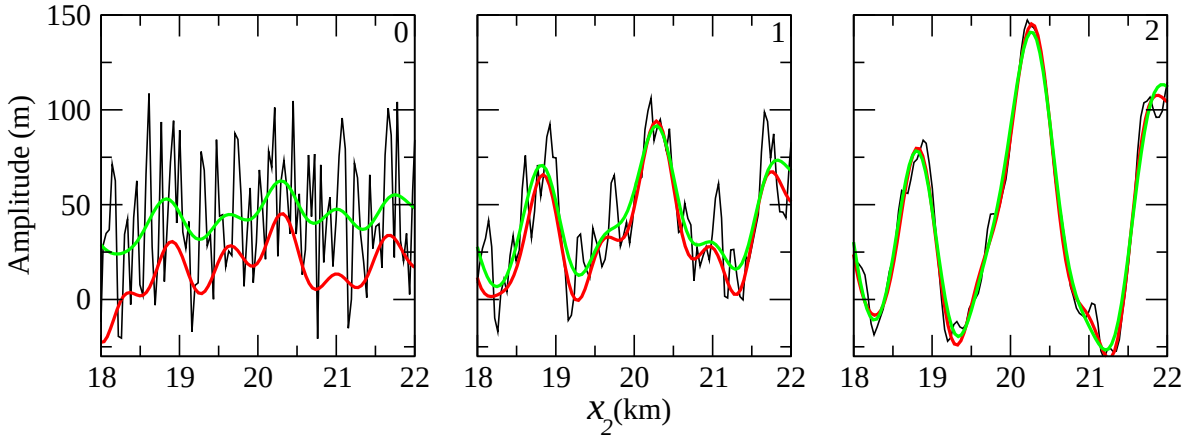

Figure 11. Sample of the three effective topographies (red lines) to compare with the original topography (black line) and the lowpass filtered topography (green line) for $\varepsilon_0 = 0.5$ and for the three tested topographies, 0 (left graph) 1 (center graph) and 2 (right graph).

the three effective topographies and average topographies are shown on Fig. 11 for $\varepsilon_0 = 0.5$. It can be observed that, if the fact that the effective topography is similar to a lower bound envelope of the original topography when the high frequencies dominate (which is the case for topography 0), it is not that obvious when the low frequency topography is significant (which is the case for topographies 1 and 2). It can nevertheless be observed that the effective topography is most of the time significantly deeper than the average topographies. Once the effective topography computed, synthetic seismograms are computed with SEM in a domain with $\mathbf{\Gamma}_a^{\varepsilon_0}$ as free boundary ("average solution") and with $\mathbf{\Gamma}_s^{\varepsilon_0}$ taking into account the order 1 DtN operator (160) ("order 1 solution"). An example of the obtained seismograms for a receiver located 28.5 km away from the source, for two values of ε_0 and for the three

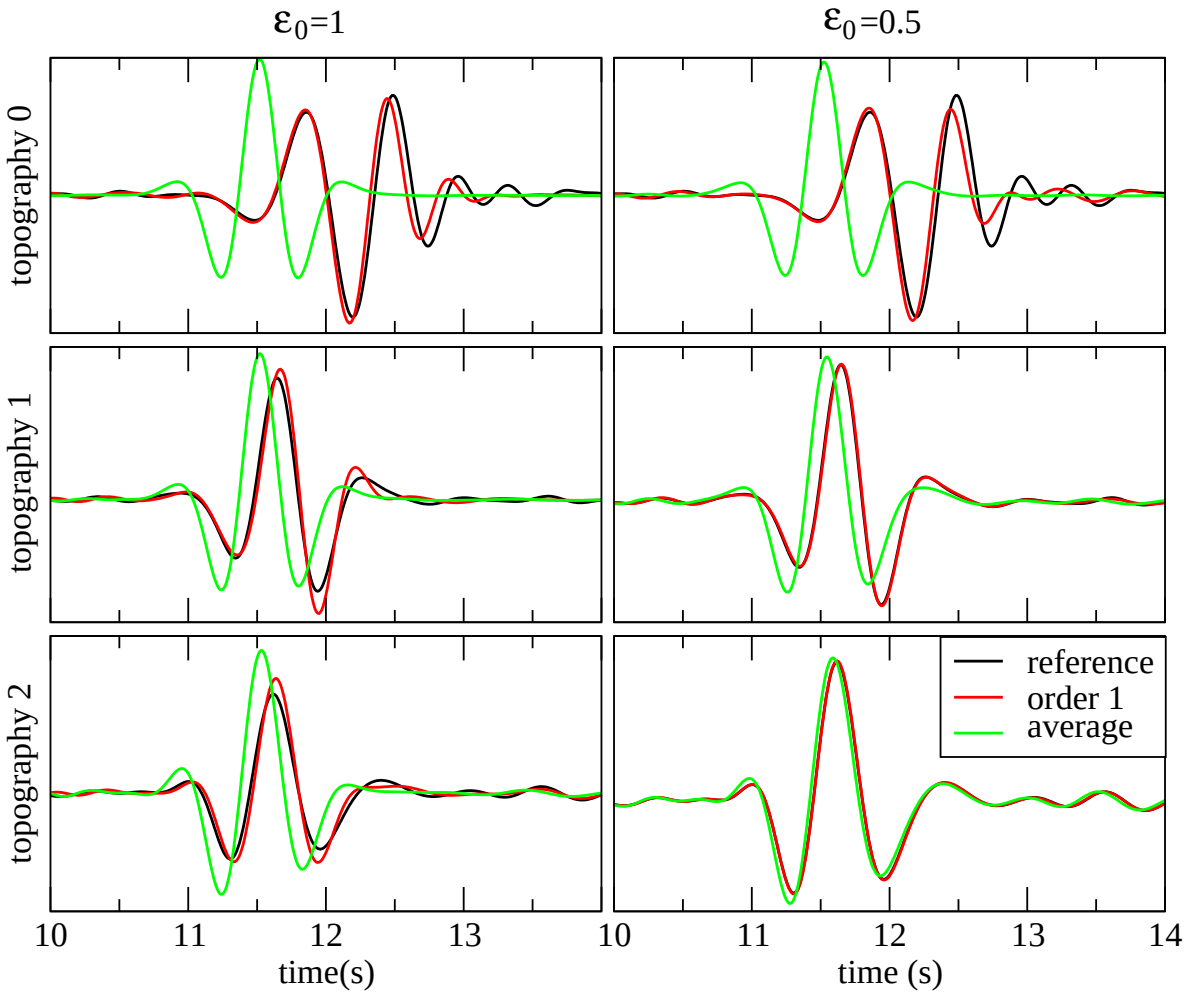

Figure 12. Examples of vertical traces computed for a receiver located at 28.5 km from the source. The reference solution (black line), the effective solution (red line) and the solution computed using the average topography $\mathbf{\Gamma}_a^{\varepsilon_0}$ (green line) are plotted for the three tested topography (topography 0: first line of graphs; topography 1: second line; topography 3: third line) and two values of ε_0 ($\varepsilon_0 = 1$: left column of graphs; $\varepsilon_0 = 0.5$: right column of graphs)

topographies is presented on Fig. 12. For the topography 0 (Fig. 12, to graphs), as expected, the average solution (an order 0 solution) doesn't seem to converge with ε. This is confirmed on Fig. 13, left graph, with the L_2 error (see (77)) as a function of ε_0 that shows little improvement with smaller ε_0. The order 1 solution significantly improves the accuracy compared to the solution computed with the average topography, but it seems that, similarly to the "average solution", little improvement of the accuracy comes with lower ε_0. Nevertheless, on the L_2 error (Fig. 13, left graph), it can be seen that, after a slow decrease for $\varepsilon_0 < 0.5$, the error of the order 1 solution decreases as fast as ε_0. This result is surprising but shows that the order 1 solution can converge in a flat Fourier spectrum topography, at least for some examples. For topography 1, both on traces (Fig. 12, middle graphs) and on the L_2

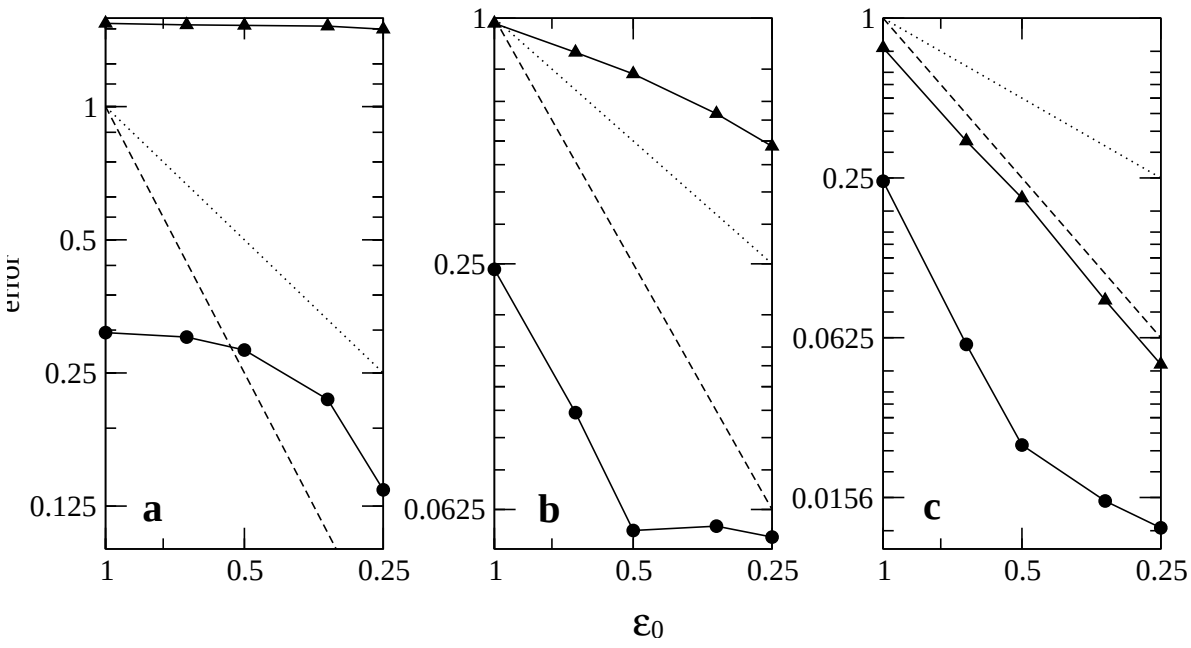

Figure 13. Graphs a,b and c: L2 errors computed following (77) as a function of ε_0 for topography 0, 1 and 2 respectively. The black circles are the errors for the effective solution developed in the present paper $\tilde{\mathbf{u}}^{\varepsilon_0,1}$ and the black triangles, the error obtained in a lowpass filtered topography (with the same filter as the one used to find the effective topography). The dotted and dashed lines display, respectively, ε_0 and ε_0^2 curves for comparison.

error (Fig. 13, center graph) a steady convergence with ε_0 of the solution computed in the average topography can be observed, which was expected. The order 1 solution shows a more accurate solution than the average solution and a ε_0^2 solution, at least for $\varepsilon_0 < 0.5$. The fact that the error doesn't continue to decrease for lower ε_0 is due to the error of the SEM itself, and to the fact that we can't use exactly the same mesh for both reference and asymptotic solutions. A solution to that problem would be to significantly decrease the element size, which we haven't done knowing the excellent accuracy already reached. For topography 2, both on traces (Fig. 12, bottom graphs) and on the L_2 error (Fig. 13, right graph), a steady convergence in ε_0^2 can be observed for the solutions computed in the average topography. For the order 1 solution, a convergence faster that ε_0^2 is observed for $\varepsilon_0 < 0.5$ and then a converge in ε_0. The change in the rate of convergence is once again probably due to the SEM error itself.

Finally, the traces presented Fig. 14 show that the difference between solutions obtained in $\mathbf{\Gamma}_a^{\varepsilon_0}$ and $\mathbf{\Gamma}_s^{\varepsilon_0}$ but with a free boundary condition ("order 0 solution") is weak. Both solutions are order 0 solutions and show the same convergence rate with ε_0. Nevertheless, the solution obtained with $\mathbf{\Gamma}_s^{\varepsilon_0}$ has a slightly better accuracy than the solution computed in the averaged topography $\mathbf{\Gamma}_a^{\varepsilon_0}$.

To conclude these tests, it can be said that the rate of convergence depends on the Fourier spectrum

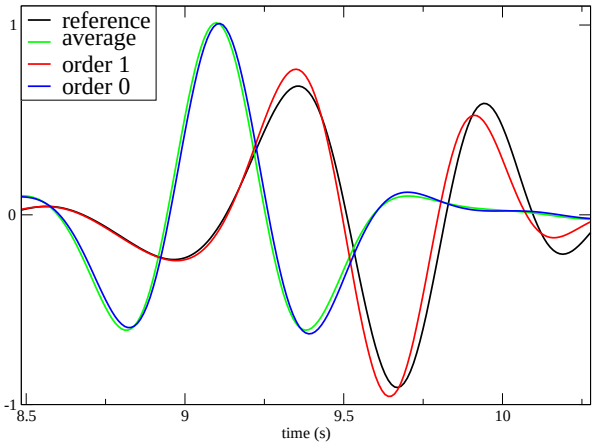

Figure 14. Example of vertical traces computed for a receiver located at 20.5 km from the source for the topography 0. The reference solution (black line), order 1 the effective solution (red line) and the solution computed using the average topography $\mathbf{\Gamma}_a^{\varepsilon_0}$ (green line) as well as the order 0 solution (blue line) are plotted for ε_0 =0.5.

of the topography, which is rather intuitive as the smallest is the amplitude of the fast scale topography the littlest effect of the fast topography is expected. Of both order 0 solutions (average topography, order 0 effective topography), the effective topography gives the best results, nevertheless, the difference is small. The order 1 solution brings a significant improvement in the accuracy of the solution and one order in ε_0 for the convergence rate.

4 DISCUSSION AND CONCLUSIONS

We have shown a two scale asymptotic method able to take into account non-periodic fast scales topography for 2D elastic waves in homogeneous media. To the order 1, the fast scale topography can be replaced by a smooth effective topography and the dynamic boundary condition. We have shown that the effective topography is approximately similar to a lower envelope of the fast topography and the dynamic boundary condition account for the inertial effect of the fast topography above the effective topography. Its overall effect is to slow down the elastic waves propagating along the topography. It can approximately said that the waves are propagating almost below the fast topography but are slowed down by the inertial effect of the weight of the fast topography above the effective free surface. We have shown that the convergence rate of the asymptotic method depends upon the Fourier spectrum of the topography: the faster it decreases with the wavenumber, the faster the method converges. A flat Fourier spectrum topography shows a poor convergence. The asymptotic method allows to build first order correctors for receivers and sources located within the fast topography. The corrector effect can be particularly large for moment tensor sources. If the algorithm proposed here to find the effective

interface allows to find an effective topography, it is not fully satisfactory. Indeed, it is iterative and implies multiple meshes. It is therefore not straightforward to implement and moreover, if the convergence is fast for the first iterations, it is then slow to achieve a more precise results. One can hope to find a more direct and effective algorithm in future.

With respect to the work of Huang & Maradudin (1987) and Mayer *et al.* (1991), which, among other results, shows that the fast topography behaves like a shallow slow layer, we can say that we find a similar result. Indeed the inertial effect of the fast topography locally increases the density in the neighborhood of the effective free surface, which decreases the elastic wave velocities. Nevertheless, this is not exactly the effect of a slow layer. Indeed, a slow thin layer has also an elastic effect (Capdeville & Marigo, 2008), which is not present here. The effect of the fast topography is therefore more a high density layer effect rather than a slow layer effect.

About Köhler *et al.* (2012)'s work, their idea is that the phase of surface waves is affected by the longer propagation path in the topography than in a flat earth. This is true for a smooth topography but not for a fast topography. Indeed, we have shown that for topographies varying faster than the minimum wavelength, the effect of the topography is dominated by the order one effect (high density layer) and not by the shape of the effective topography (see Fig. 14). Depending on the Fourier spectrum characteristic of the actual topography, the bias introduced by the fast topography is important or negligible. A systematic study of the fast topography effect remains to be done for the real earth, nevertheless, this effect is expected to be small for large or regional scale (let say 10000 km to 10 km), but maybe not at small scales (surface waves propagating through in a city with large buildings for example).

The general 2-D case, i.e. fast topography and fast elastic and density property variations as well as the 3-D case still need to be treated. The relevance of our iterative algorithm to find the effective topography in the inhomogeneous 3-D case will have to be demonstrated and probably adapted.

Homogenization and upscaling in general have a lot to do with the inverse problem (tomography) in seismology. The result of an elastic inversion of seismic data is closely related to the homogenized version of the real earth. In general, the present work should impact inversion technique and the interpretation of tomographic images. Indeed, for a given frequency band, the known fine scale topography should be upscaled to the actual scale of the inversion and the boundary condition modified in order to avoid miss-interpretation of a slow layer in the near surface. In practice, even if this remains to be closely studied, for most of the earth locations, the topography spectrum and amplitude is probably such that these effects are small.

5 ACKNOWLEDGMENTS

We thank Valerie Maupin for an interesting discussion about the effect of topography on surface waves. We thank Gaetano Festa for letting use and modify his 2-D spectral element program. This work was supported by the ANR Blanche mémé.

REFERENCES

Boutin, C. & Roussillon, P., 2006. Wave propagation in presence of oscillators on the free surface. *Int. J. Engng. Sci*,, **44**, 180–204.

Capdeville, Y., Guillot, L. & Marigo, J. J., 2010a. 1-D non periodic homogenization for the wave equation. *Geophys. J. Int.*, **181**, 897–910.

Capdeville, Y., Guillot, L. & Marigo, J. J., 2010b. 2D nonperiodic homogenization to upscale elastic media for P-SV waves. *Geophys. J. Int.*, **182**, 903–922.

Capdeville, Y. & Marigo, J. J., 2007. Second order homogenization of the elastic wave equation for non-periodic layered media. *Geophys. J. Int.*, **170**, 823–838.

Capdeville, Y. & Marigo, J. J., 2008. Shallow layer correction for spectral element like methods. *Geophys. J. Int.*, **172**, 1135–1150.

Chaljub, E., Komatitsch, D., Capdeville, Y., Vilotte, J.-P., Valette, B. & Festa, G., 2007. Spectral element analysis in seismology. In R.-S. Wu & V. Maupin (Eds.), *Advances in Wave Propagation in Heterogeneous Media*, Volume 48 of *Advances in Geophysics Series*, pp. 365–419. Elsevier.

Chechkin, G., Friedman, A. & Piatnitski, A., 1996, December. The Boundary-Value Problem in Domains with Very Rapidly Oscillating Boundary. Technical Report RR-3062, INRIA.

David, M., Marigo, J.-J. & Pideri, C., 2012. Homogenized interface model describing inhomogeneities located on a surface. *Journal of Elasticity*, **xx**, xx–xx.

Dumontet, H., 1990. *Homogénéisation et effets de bords dans les materiaux composites*. Ph. D. thesis, Univertité Paris 6.

Eger, V., Oleinik, O. A. & Shaposhnikova, T. A., 2000. Homogenization of boundary value problems in domains with rapidly oscillating nonperiodic boundary. *Differential Equations 36*(6), 833–846.

Festa, G., Delavaud, E. & Vilotte, J.-P., 2005. Interaction between surface waves and absorbing boundaries for wave propagation in geological basins: 2D numerical simulations. *Geophys. Res. Lett.*, **32**, L20306.

Fish, J. & Chen, W., 2004. Space-time multiscale model for wave propagation in heterogeneous media. *Comp. Meth. Appl. Mech. Engng*, **193**, 4837–4856.

Fletcher, C., 1991. *Computational Fluid Dynamics*. Springer Verlag,New York, NY.

Geuzaine, C. & Remacle, J.-F., 2009. Gmsh: a three-dimensional finite element mesh generator with built-in pre- and post-processing facilities. *Int. J. Num. Methods in Engrg.*, **79**, 1309–1331.

Grisvard, P., 1985. *Elliptic problems in non smooth domains*. Number 24 in Monographs and Studies in Mathematics. Pitman.

Guillot, L., Capdeville, Y. & Marigo, J. J., 2010. 2-D non periodic homogenization for the SH wave equation. *Geophys. J. Int.*, **182**, 1438–1454.

Huang, X. & Maradudin, A. A., 1987. Propagation of surface acoustic waves across random gratings. *Phys Rev B 36*(15), 7827–7839.

Köhler, A., Weidle, C. & Maupin, V., 2012. On the effect of topography on surface wave propagation in the ambient noise frequency range. *Journal of Seismology*, **16**, 221–231.

Komatitsch, D., Coutel, F. & Mora, P., 1996. Tensorial formulation of the wave equation for modelling curved interfaces. *Geophys. J. Int. 127*(1), 156–168.

Komatitsch, D. & Vilotte, J. P., 1998. The spectral element method: an effective tool to simulate the seismic response of 2D and 3D geological structures. *Bull. Seism. Soc. Am.*, **88**, 368–392.

Maradudin, A., Huang, X. & Mayer, A., 1991. Propagation of shear horizontal surface acoustic waves parallel to the grooves of a random grating. *J. App. Physics 70*(1), 53–62.

Marigo, J. & Pideri, C., 2011. The effective behavior of elastic bodies containing microcracks or microholes localized on a surface. *International Journal of Damage Mechanics*.

Mayer, A., Zierau, W. & Maradudin, A., 1991. Surface acoustic waves propagating along the grooves of a periodic grating. *J. App. Physics 69*(4), 1942–1947.

Mercerat, E. D., Vilotte, J. P. & Sánchez-Sesma, F. J., 2006. Triangular spectral element simulation of two-dimensional elastic wave propagation using unstructured triangular grids. *Geophys. J. Int.*, **166**, 679–698.

Nevard, J. & Keller, J. B., 1997. Homogenization of rough boundaries and interfaces. *J. Appl. Math 67*(6), 1660–1686.

Pasquetti, R. & Rapetti, F., 2004. Spectral element methods on triangles and quadrilaterals: comparisons and applications. *J. Comp. Phys.*, **198**, 349–362.

Rathod, H., abd B. Ventkatesudu, K. V. N. & Ramesh, N. L., 2004. Gauss legendre quadrature over a triangle. *J. Indian Inst. Sci.*, **84**, 183–188.

Sanchez-Palencia, E., 1986. Elastic body with defects distributed near a surface. In *Homogenization Techniques for Composite Media*. Springer Verlag.

APPENDIX A: SOME NOTATIONS USED THROUGHOUT THE PAPER

For any 4th-order tensor $\mathbf{A}$ and second order tensor $\mathbf{b}$, we note

$$[\mathbf{A} : \mathbf{b}]_{ij} \equiv A_{ijkl} b_{kl} \,, \tag{A1}$$

where the sum over repeated subscripts is assumed. For any 4th-order tensors $\mathbf{A}$ and $\mathbf{B}$, we note

$$[\mathbf{A} : \mathbf{B}]_{ijkl} \equiv A_{ijmn} B_{mnkl} \,. \tag{A2}$$

We will sometimes use the following compact notation for partial derivatives with respect to any variable x of a given function u:

$$\partial_x u \equiv \frac{\partial u}{\partial x} \,, \tag{A3}$$

and the classical notation for time partial derivative: for any u

$$\dot{u} \equiv \frac{\partial u}{\partial t} \,. \tag{A4}$$

We define the gradient, for any vector $\mathbf{u}$,

$$\boldsymbol{\nabla} \mathbf{u} \equiv \frac{\partial u_i}{\partial x_j} \, \hat{\mathbf{x}}_i \otimes \hat{\mathbf{x}}_j \,, \tag{A5}$$

where $\hat{\mathbf{x}}_i$, $i = 1, 2$ are the unit vector of the Cartesian coordinate system and $\otimes$ the tensor product. We define the divergence, for any tensor $\boldsymbol{\tau}$,

$$\boldsymbol{\nabla} \cdot \boldsymbol{\tau} \equiv \frac{\partial \tau_{ij}}{\partial x_j} \, \hat{\mathbf{x}}_i \,, \tag{A6}$$

the gradient along a single component

$$\boldsymbol{\nabla}_{x_\alpha} \mathbf{u} \equiv \frac{\partial u_i}{\partial x_\alpha} \, \hat{\mathbf{x}}_\alpha \otimes \hat{\mathbf{x}}_i \quad \text{(no sum on } \alpha\text{)}, \tag{A7}$$

as well as the divergence along a single component

$$\boldsymbol{\nabla}_{x_\alpha} \cdot \boldsymbol{\tau} \equiv \frac{\partial \tau_{\alpha i}}{\partial x_\alpha} \, \hat{\mathbf{x}}_i \quad \text{(no sum on } \alpha\text{)}. \tag{A8}$$

We define the strain tensor,

$$\boldsymbol{\epsilon}(\mathbf{u}) \equiv \frac{1}{2} \left(\frac{\partial u_i}{\partial x_j} + \frac{\partial u_j}{\partial x_i} \right) \, \hat{\mathbf{x}}_i \otimes \hat{\mathbf{x}}_j \,, \tag{A9}$$

as well as the strain tensor with respect to a single component

$$\boldsymbol{\epsilon}_{x_\alpha}(\mathbf{u}) \equiv \frac{1}{2} \left(\frac{\partial u_i}{\partial x_\alpha} \, \hat{\mathbf{x}}_\alpha \otimes \hat{\mathbf{x}}_i + \frac{\partial u_j}{\partial x_\alpha} \, \hat{\mathbf{x}}_j \otimes \hat{\mathbf{x}}_\alpha \right) \quad \text{(no sum on } \alpha\text{)}. \tag{A10}$$

APPENDIX B: MATCHING CONDITIONS FOR THE NON-PERIODIC CASE

To establish the matching conditions between the two asymptotic expansions, we assume that it exists an area where both are valid: for a given $\mathbf{x} \in \mathbf{\Gamma}_s^{\varepsilon_0}$, we assume it exits a large enough y_1 such that both expansion are valid for $\mathbf{x} + \boldsymbol{\zeta}_{\varepsilon_0}(\varepsilon \mathbf{y})$:

$$\begin{aligned} \lim_{y_1 \to \infty} \mathbf{v}^\varepsilon(z_2, y_1, y_2) &= \mathbf{u}^\varepsilon(\mathbf{x} + \boldsymbol{\zeta}_{\varepsilon_0}(\varepsilon \mathbf{y}))\,, \\ \lim_{y_1 \to \infty} \boldsymbol{\tau}^\varepsilon(z_2, y_1, y_2) &= \boldsymbol{\sigma}^\varepsilon(\mathbf{x} + \boldsymbol{\zeta}_{\varepsilon_0}(\varepsilon \mathbf{y}))\,, \end{aligned} \tag{B1}$$

where z_2 is the $\mathbf{x}$ curvilinear position along $\mathbf{\Gamma}_s^{\varepsilon_0}$. When ε goes toward zero, even if y_1 is large, $\varepsilon \mathbf{y}$ is small and, for any i, a Taylor expansion can be done:

$$\boldsymbol{\zeta}_{\varepsilon_0}(\varepsilon \mathbf{y}) = \sum_{i=1}^{\infty} \frac{\varepsilon^i}{i!} y_1^i \partial_{z_1}^i \boldsymbol{\zeta}_{\varepsilon_0}(0, y_2)\,. \tag{B2}$$

Knowing that $\mathbf{g}_1(\mathbf{x}) = \partial_{z_1} \boldsymbol{\zeta}_{\varepsilon_0}|_{\mathbf{z}=\varepsilon(0,y_2)}$ for $\mathbf{x} = \boldsymbol{\zeta}_{\varepsilon_0}(\varepsilon(0, y_2))$, we have

$$\boldsymbol{\zeta}_{\varepsilon_0}(\varepsilon \mathbf{y}) = \sum_{i=1}^{\infty} \frac{\varepsilon^i}{i!} y_1^i \mathbf{g}_1^i\,, \tag{B3}$$

where $\mathbf{g}_1^i = \partial_{z_1}^{i-1} \mathbf{g}_1$. For any small vector $\mathbf{a}$, we have

$$\mathbf{u}^i(\mathbf{x} + \mathbf{a}, \mathbf{y}) = \sum_{j=0}^{\infty} \left[\frac{1}{j!} (\mathbf{a} \cdot \boldsymbol{\nabla}_{\mathbf{x}})^j \mathbf{u}^i(\mathbf{x}, \mathbf{y}) \right]\,. \tag{B4}$$

Combining (B3) and (B4), at the order 2, we find

$$\begin{aligned} \mathbf{u}^i(\mathbf{x} + \boldsymbol{\zeta}_{\varepsilon_0}(\varepsilon \mathbf{y})) = \mathbf{u}^i(\mathbf{x}) &+ \varepsilon y_1 \left(\mathbf{g}_1 \cdot \boldsymbol{\nabla}_{\mathbf{x}}\right) \mathbf{u}^i(\mathbf{x}) \\ &+ \frac{1}{2} \varepsilon^2 y_1^2 \left(\left(\partial_{z_1} \mathbf{g}_1 \cdot \boldsymbol{\nabla}_{\mathbf{x}}\right) + \left(\mathbf{g}_1 \cdot \boldsymbol{\nabla}_{\mathbf{x}}\right)^2 \right) \mathbf{u}^i(\mathbf{x}) + O(\varepsilon^3) \end{aligned} \tag{B5}$$

Applying the same taylor expansion to $\boldsymbol{\sigma}^i$, combining the last equation with B1, identifying terms by power of ε yields:

- order 0:

$$\begin{aligned} \lim_{y_1 \to \infty} \mathbf{v}^0(z_2, y_1, y_2) &= \mathbf{u}^0(\mathbf{x})\,, \\ \lim_{y_1 \to \infty} \boldsymbol{\tau}^0(z_2, y_1, y_2) &= \boldsymbol{\sigma}^0(\mathbf{x})\,; \end{aligned} \tag{B6}$$

- order 1:

$$\begin{aligned} \lim_{y_1 \to \infty} \mathbf{v}^1(z_2, y_1, y_2) &= \mathbf{u}^1(\mathbf{x}) + y_1 \left(\mathbf{g}_1 \cdot \boldsymbol{\nabla}_{\mathbf{x}}\right) \mathbf{u}^0(\mathbf{x})\,, \\ \lim_{y_1 \to \infty} \boldsymbol{\tau}^1(z_2, y_1, y_2) &= \boldsymbol{\sigma}^1(\mathbf{x}) + y_1 \left(\mathbf{g}_1 \cdot \boldsymbol{\nabla}_{\mathbf{x}}\right) \boldsymbol{\sigma}^0(\mathbf{x})\,; \end{aligned} \tag{B7}$$

- order 2:

$$\begin{aligned}\lim_{y_1\to\infty}\mathbf{v}^2(z_2,y_1,y_2) &= \mathbf{u}^2(\mathbf{x}) + y_1\left(\mathbf{g}_1\cdot\boldsymbol{\nabla}_{\mathbf{x}}\right)\mathbf{u}^1(\mathbf{x}) \\ &\quad + \frac{1}{2}y_1^2\left(\left(\partial_{y_1}\mathbf{g}_1\cdot\boldsymbol{\nabla}_{\mathbf{x}}\right) + \left(\mathbf{g}_1\cdot\boldsymbol{\nabla}_{\mathbf{x}}\right)^2\right)\mathbf{u}^0(\mathbf{x})\,, \\ \lim_{y_1\to\infty}\boldsymbol{\tau}^2(z_2,y_1,y_2) &= \boldsymbol{\sigma}^2(\mathbf{x}) + y_1\left(\mathbf{g}_1\cdot\boldsymbol{\nabla}_{\mathbf{x}}\right)\boldsymbol{\sigma}^1(\mathbf{x}) \\ &\quad + \frac{1}{2}y_1^2\left(\left(\partial_{y_1}\mathbf{g}_1\cdot\boldsymbol{\nabla}_{\mathbf{x}}\right) + \left(\mathbf{g}_1\cdot\boldsymbol{\nabla}_{\mathbf{x}}\right)^2\right)\boldsymbol{\sigma}^0(\mathbf{x})\,.\end{aligned} \tag{B8}$$

We obtain the periodic case matching asymptotic conditions by using $\boldsymbol{\zeta}_{\varepsilon_0}(\mathbf{z}) = \mathbf{z}$.

APPENDIX C: RELATION BETWEEN FILTERED T_{22} AND Γ^{ε_0}

We first define the scalar function

$$W(y_2) = \int_0^{y_2} w_m(y_2')\,dy_2'\,, \tag{C1}$$

such

$$w_m(y_2)\hat{\mathbf{y}}_2 = \boldsymbol{\nabla}_{\mathbf{y}}W\,. \tag{C2}$$

Using an integration by parts and the equilibrium equation of the cell problem (138), we have

$$\int_{\mathbb{Y}} W\boldsymbol{\nabla}_{\mathbf{y}}\cdot\mathbf{T}\,d\mathbf{y} = \int_{\partial\mathbb{Y}} W\mathbf{T}\cdot\mathbf{n}\,d\mathbf{y} - \int_{\mathbb{Y}} w_m\,\hat{\mathbf{y}}_2\cdot\mathbf{T}\,d\mathbf{y} = \mathbf{0}\,. \tag{C3}$$

Taking advantage of the periodicity in y_2, of the boundary condition in $y_1\to\infty$ and on $\boldsymbol{\Gamma}^{\varepsilon_0}$, we have

$$\int_{\mathbb{Y}} w_m T_{21}\,d\mathbf{y} = 0\,, \tag{C4}$$

$$\int_{\boldsymbol{\Gamma}^{\varepsilon_0}} W n_2\,d\mathbf{y} + \int_{\mathbb{Y}} w_m T_{22}\,d\mathbf{y} = 0\,. \tag{C5}$$

Reminding that $\boldsymbol{\Gamma}^{\varepsilon_0} = \{\mathbf{y}\in\mathbb{Y}; y_1 = \Gamma^{\varepsilon_0}(y_2)\}$, we have

$$n_2 = -\frac{\partial\Gamma^{\varepsilon}}{\partial s}\,, \tag{C6}$$

where $s(y_2) = \int_0^{y_2}\Gamma^{\varepsilon_0}(y_2')\,dy_2'$. Therefore,

$$\int_{\boldsymbol{\Gamma}^{\varepsilon_0}} W n_2\,d\mathbf{y} = -\int_0^{s_m} W\frac{\partial\Gamma^{\varepsilon}}{\partial s}\,ds\,, \tag{C7}$$

$$= -\int_0^{Y_w} W\frac{\partial\Gamma^{\varepsilon}}{\partial y_2}\,dy_2\,, \tag{C8}$$

$$= \int_0^{Y_w} w_m\Gamma^{\varepsilon}\,dy_2\,. \tag{C9}$$

Finally, we have, using $w_m(y_2' - y_2)$ instead of $w_m(y_2)$ in the above development

$$\bar{\mathcal{F}}\left(T_{22}\right) = -\mathcal{F}\left(\Gamma^{\varepsilon_0}\right) \,, \tag{C10}$$

$$\bar{\mathcal{F}}\left(T_{21}\right) = 0 \,, \tag{C11}$$

where, for any scalar $t(\mathbf{y})$,

$$\bar{\mathcal{F}}\left(t\right)\left(y_2\right) = \int_{\mathbb{Y}} w_m(y_2 - y_2') t(y_1', y_2') \, d\mathbf{y}' \,. \tag{C12}$$